

Minimal Dark Matter: Generalized Framework and Direct-Detection Sensitivity

Spencer Griffith ^{1,2,*} Juri Smirnov ^{3,†} Laura Lopez-Honorez ^{4,5,‡} and John F. Beacom ^{1,2,6,§}

¹*Center for Cosmology and AstroParticle Physics (CCAPP), Ohio State University, Columbus, OH 43210*

²*Department of Physics, Ohio State University, Columbus, OH 43210*

³*Department of Mathematical Sciences, University of Liverpool, Liverpool, L69 7ZL, United Kingdom*

⁴*Service de Physique Théorique, Université Libre de Bruxelles, B-1050 Brussels, Belgium*

⁵*Theoretische Natuurkunde & The International Solvay Institutes,*

Vrije Universiteit Brussel, B-1050 Brussels, Belgium

⁶*Department of Astronomy, Ohio State University, Columbus, OH 43210*

(Dated: February 23, 2026)

Minimal electroweak dark matter models are compelling due to their simplicity, though calculations of their freezeout abundance are complicated by nonperturbative effects due to Sommerfeld enhancement and bound-state formation. It has been shown that all individual multiplet scenarios beyond the doublet lead to direct-detection signals above the neutrino floor and thus within the reach of next-generation experiments. If no signals are found, would minimal dark matter be excluded? Yes for the simplest models, but it has been unknown for the important extension of two multiplets coupled by Higgs interactions (Higgs-coupled minimal dark matter). We present a generalized framework for calculating nonperturbative effects for such models that also covers the case of individual multiplets. In this framework, we calculate nonperturbative effects on freezeout as well as the prospects for direct detection, correcting shortcomings and omissions in the literature. Importantly, for the mixed Majorana (odd) and Dirac (even) multiplet combinations $3M2D$, $5M4D$, and $7M6D$, we find that the predicted direct-detection signals can extend below the neutrino floor. *Fully testing minimal dark matter will thus require more than direct-detection experiments.*

I. INTRODUCTION

The particle nature of dark matter (DM) is one of the longest-running questions in physics [1]. The resolution of this question will have profound implications. For particle physics, understanding DM will reveal physics beyond the standard model (BSM); for examples, see Refs. [2–7]. For cosmology, understanding DM is crucial for understanding the overall evolution of the universe and the clustering of matter, see e.g. Refs. [8–12].

Minimal dark matter (MDM) [4, 13, 14] is an especially attractive class of weakly interacting massive particle (WIMP) models [15–19]. These models take the WIMP miracle seriously and propose that DM is a component of an electroweak $SU(2)_L$ multiplet that can be added to the standard model (SM) with little fuss. At tree level, calculation of the the DM annihilation cross section to SM particles and the DM freezeout abundance is simple [13]. However, because the DM masses are typically quite large, the weak bosons appear relatively massless, which makes it important to account for nonperturbative effects on the cross section due to Sommerfeld enhancement and bound-state formation. This is analogous to the enhancement of $e^+ + e^-$ annihilation due to the attractive Coulomb potential and positronium formation [20]. The Sommerfeld effect for DM has been calculated in, e.g., Refs. [21–25], while bound-state effects

have been calculated in, e.g., Refs. [26–29]. A distinctive aspect of MDM models is that they appear to be fully testable by next-generation direct-detection experiments [30–32]. Furthermore, current bounds from direct detection eliminate even multiplets due to their tree level coupling to the Z [33, 34], though this can be evaded by adding interactions beyond those of strictly MDM (see, e.g., Ref. [12]).

Higgs-coupled minimal dark matter (HC-MDM) is a modest and important extension to this model. Here, DM is a combination of two different multiplets that couple through the Higgs. This is the simplest way of introducing Higgs-mediated interactions for fermionic DM, thus making use of all the players in the electroweak sector. This model is still minimal in the sense that it contains only $SU(2)_L$ couplings. In Ref. [35], it was shown that if one combines two multiplets with a dimension difference of one and at most a small mass difference, the resulting mixed state behaves like an odd multiplet. Under certain constraints, these particles can have large Higgs couplings while still evading direct-detection constraints. However, large Higgs couplings have a profound effect on the annihilation cross section through Sommerfeld effects and bound-state formation. This has not been well explored. For this model, Ref. [35] calculated the Sommerfeld effect but only roughly estimated bound-state formation effects. Then, in Refs. [36, 37], these nonperturbative effects were calculated in detail, but only for the singlet-doublet case.

In this paper, our goal is to systematically explore mixed-multiplet HC-MDM models for higher multiplets, to calculate the effects on the freezeout predictions, and to assess how well these models can be probed by direct-

* griffith.1037@osu.edu

† juri.smirnov@liverpool.ac.uk

‡ Laura.Lopez.Honorez@ulb.be

§ beacom.7@osu.edu

detection experiments. This is significantly different from the exclusively singlet-doublet case considered in Refs. [36, 37] because the singlet has no $SU(2)_L$ coupling, which means that the potentials and cross sections lack some features found in larger multiplet combinations. We begin by establishing the first complete framework for HC-MDM calculations, accounting for Sommerfeld and bound-state effects on DM freezeout and thus the allowed DM masses. Our framework, which corrects various shortcomings and omissions in the literature, also applies (in appropriate limits) to MDM with single multiplets. We reproduce previous results for the prediction of MDM masses [29, 30, 38, 39] up to the 13-plet, which is the limiting representation due to unitarity constraints [30, 39]. With our framework established, we address the key questions of the paper: *what masses are required for HC-MDM to comprise the entirety of observed DM and what are the direct-detection prospects for HC-MDM models?*

The remainder of this paper is organized as follows. In Sec. II, we review the MDM and HC-MDM models as well as establish notation that will be used throughout. In Sec. III, we present our formalism for determining the freezeout abundance and accounting for nonperturbative effects. In Sec. IV, we calculate the long-range potentials of the DM particles that generate the nonperturbative corrections) as well as the annihilation cross sections. In Sec. V, we find the Sommerfeld-enhanced annihilation cross section of scattering states. In Sec. VI, we determine the cross sections for bound-state formation. In Sec. VII, we apply these calculations to specific multiplet combinations to determine the DM masses and discuss the implications for direct detection. Finally, in Sec. VIII we conclude and discuss ways forward.

II. MDM AND HC-MDM MODELS

In this section, we review the MDM and HC-MDM models and discuss some current experimental constraints. We also introduce the simplifications that we use in the remainder of our discussion. Finally, we establish the notation used in the following sections.

The MDM model proposes adding a single $SU(2)_L$ multiplet to the SM Lagrangian, which may be either a scalar or a fermion. We focus on the fermion case. (In the scalar case, the Higgs portal does not need the introduction of a second multiplet [13, 40].) The SM Lagrangian is modified by adding the term:

$$\mathcal{L} = \mathcal{L}_{\text{SM}} + C\bar{X}(i\not{\partial} + m_X)X, \quad (1)$$

where $\not{\partial}$ is the covariant derivative, m_X is the mass of the DM particle X , and $C = 1/2$ for self-conjugate (Majorana) X or $C = 1$ for non self-conjugate (Dirac) X .

The distinction between the Majorana and Dirac cases depends on the assignment of the weak hypercharge (Y_X), because a particle with $Y_X \neq 0$ clearly cannot be its own antiparticle. DM with non-zero hypercharge is already

ruled out by direct-detection experiments (or minimality must be abandoned to appropriately cancel the offending interactions [33, 34]). Furthermore, from the Gell-Mann–Nishijima relation:

$$Q_X = I_X^3 + Y_X, \quad (2)$$

where Q_X is the electric charge and I_X^3 is the 3rd component of isospin, we see that Y_X is constrained by the requirement that one component of the multiplet is electrically neutral and, consequently, that only odd multiplets can meet the requirement of $Y_X = 0$. Additionally, multiplets of dimension five or greater are stable against decay to the SM, while smaller multiplets can be stable if we impose a symmetry under which the DM is odd and the SM is even [13].

Reference [13] showed that odd multiplets of dimension greater than five produce a Landau pole below the Planck mass. However, this does not rule out these multiplets. Instead, it points to the necessity for a UV completion scenario that eliminates the offending operators [30]. Furthermore, Ref. [39] proposes a solution based on resummation techniques. We can, however, determine an upper limit on the multiplet size by demanding s -wave unitarity of the cross section. Under this constraint, multiplets up to the 13-plet are acceptable DM candidates [30, 39].

The odd multiplets up to the 13-plet lie slightly below current direct-detection bounds. Conveniently, as shown in Ref. [30], they also lie above the “neutrino floor,” the combination of cross section and mass below which neutrino backgrounds make direct detection extremely difficult [41]. The proposed next generation of direct-detection experiments (such as XLZD [32]) will probe down to neutrino floor. Indirect-detection bounds also put pressure on MDM models, as recent analyses of Fermi data (see e.g. Refs. [42, 43]) strongly disfavor the pure triplet scenario, even considering a large Milky way core. For larger multiplets, the exclusion bounds are less stringent as they depend on the exact DM mass and the core radius [43]. Furthermore, Ref. [44] finds that the upcoming Cherenkov Telescope Array Observatory (CTAO) can test up to the 11-plet and place strong pressure on the 13-plet.

In the HC-MDM model, we add Majorana *and* Dirac fermions to \mathcal{L}_{SM} (M and D , respectively) with multiplet sizes differing by one. By requiring each multiplet to generically have a neutral member, we must have $Y_M = 0$ and $Y_D = 1/2$. The Lagrangian then acquires the terms:

$$\begin{aligned} \mathcal{L} = & \mathcal{L}_{\text{SM}} + \bar{D}(i\not{\partial} + m_D)D + \frac{1}{2}\bar{M}(i\not{\partial} + m_M)M \\ & - y_1 DMH^* - y_2 \bar{D}MH, \end{aligned} \quad (3)$$

which exhausts the possible M , D interactions. As mentioned, if the representation size of either is less than five, we must impose an additional discrete symmetry to prevent decay.

Figure 1 illustrates the transition from MDM to HC-MDM and highlights some important differences. Our

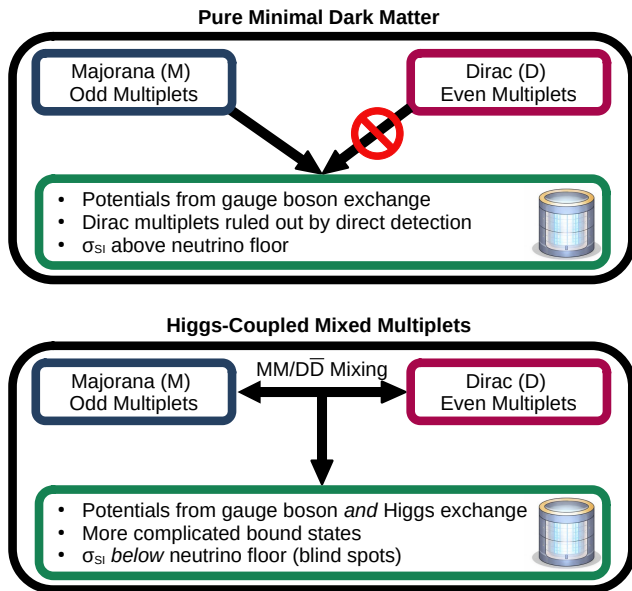


FIG. 1. Schematic diagram illustrating the salient differences between the MDM and HC-MDM models.

assertion that the HC-MDM parameter space can extend below the neutrino floor is demonstrated in Sec. VII.

As shown in Ref. [35], for M , D to mix to a combined state where the lightest neutral particle behaves as a Majorana fermion, we must have $|y_1| \approx |y_2|$. Furthermore, when $y_1 = -y_2$ and $m_D = m_M$, the tree-level coupling of the DM component to the Higgs is zero. This avoids Higgs induced DM scattering on nucleons that would add to the unavoidable next-to-leading order contributions to the scattering cross-section from gauge boson exchanges for electroweak DM [45] (see e.g., early studies of “blind spots” within the singlet-doublet model [35, 46–48]). Therefore, to simplify our calculations, we consider the case where $|y_1| = |y_2| = y$ and $m_M = m_D = m$. When we consider cases with non-negligible Higgs coupling, we impose the requirement that y_1 and y_2 have opposite sign. Below, y is always taken to be positive and any necessary negative signs are introduced manually at appropriate stages of the derivation.

These simplifications make sense when we consider mixed multiplets in generality. In Sec. VII, we choose reference values of $y_{1,2}$ to demonstrate the magnitude of the nonperturbative effects on freezeout abundance. However, if one has a particularly well-motivated model that includes specific values of $y_{1,2}$ and $m_{M,D}$, then it is straightforward to generalize our results, albeit with increased complexity and computational expense.

We also work in unbroken $SU(2)_L$ symmetry. This is because of our focus on the annihilation rates in the early universe to determine the relic abundance. We justify this in Sec. VII.

For convenience, we summarize our notation:

- X is a generic DM multiplet (M or D).

- R_X is the representation size of the X multiplet.
- g_X is the degrees of freedom of X ($2R_X$ and $4R_X$ for Majorana and Dirac particles, respectively).
- I_X is the isospin of X .
- $I_X^3(n)$ is the 3 component of isospin of the n th element of X in ascending order. For example, for a triplet X , $I_X^3(1, 2, 3) = -1, 0, 1$.
- t_X^a is the a -th $SU(2)$ generator of size of the representation of X .
- $C_2(R_X)$ is the quadratic Casimir of R_X .
- V is a non-relativistic potential (the r dependence is generally omitted). When necessary, a superscript indicates the representation size and subscripts indicate particles involved (e.g., $V_{X_1 X_2}^R$).
- For a process that changes the particle content (e.g., $X_1 + X_2 \rightarrow X_3 + X_4$), we use $X_1 X_2; X_3 X_4$.
- The coupling strength α is defined by $V = -\alpha/r$, with $\alpha_{1,2}$ the $U(1)_Y$ and $SU(2)_L$ gauge couplings and $\alpha_H = y^2/4\pi$.
- Clebsch-Gordon (CG) coefficients are written $\langle J, M | j_1, m_1; j_2, m_2 \rangle$, where J, j_i denote angular momentum quantum numbers and M, m_i the projections onto the z -axis.
- $\hat{\epsilon}_X$ is the generalization of the Levi-Civita symbol to the dimension of X used to contract indices (see Appendix B), e.g.:

$$\hat{\epsilon}_3 = \begin{pmatrix} 0 & 0 & 1 \\ 0 & -1 & 0 \\ 1 & 0 & 0 \end{pmatrix}.$$
- Latin subscripts denote a multiplet component (e.g., D_i).
- Lower case s generally denotes spin. However, s will also be used for entropy density in Sec. III.
- Upper case S is the Sommerfeld factor (see Sec. V).
- Cross sections are specified by s and I : ${}^s(\sigma_{v_{\text{rel}}})^I$.
- n_f is the number of SM fermions.
- IS and FS denote initial and final states. BS denotes a bound state.
- $z = m/T$ is a dimensionless time variable, where T is the temperature and z_f denotes z at the freezeout temperature. Note that z is *not* used for redshift.

III. FREEZEOUT ABUNDANCE FORMALISM

In this section, we summarize results necessary for calculating the relic abundance of DM from the annihilation and bound state formation cross sections. We also justify the simplifications used to make the calculation of the relic abundance tenable.

The relic abundance of electroweak DM is determined by its chemical decoupling from the SM plasma. We describe the evolution of the DM abundance using the comoving abundance $Y_{DM} = n_{DM}/s$, where n_{DM} is the number density and $s = (2\pi^2/45)g_*T^3$ is the entropy density. In terms of Y_{DM} , the Boltzmann equation is

$$\frac{dY_{DM}}{dz} = -\frac{s}{zH} \langle \sigma v_{\text{rel}} \rangle_{\text{eff}} (Y_{DM}^2 - Y_{DM,\text{eq}}^2), \quad (4)$$

where H is the Hubble rate during radiation domination, $H = 1.66 g_*^{1/2} T^2 / M_{\text{Pl}}$. Here, $\langle \sigma v_{\text{rel}} \rangle_{\text{eff}}$ is the effective thermally averaged inelastic cross section for annihilation to the SM (including nonperturbative effects) (see Refs. [29, 39, 49–51]):

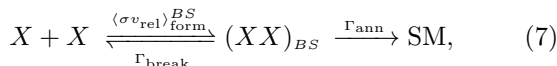
$$\langle \sigma v_{\text{rel}} \rangle_{\text{eff}} = \langle \sigma v_{\text{rel}} \rangle_{\text{ann}} + \sum_{BS_i} \langle \sigma v_{\text{rel}} \rangle_{\text{form}}^{BS_i} BR(BS_i; SM). \quad (5)$$

The first term corresponds to the Sommerfeld-enhanced annihilation of free XX pairs, while the second term accounts for the formation of unstable XX bound states (BS_i) that subsequently decay to the SM with branching ratio $BR(BS_i; SM)$. The branching ratio is given by

$$\begin{aligned} BR(BS_i; SM) &= \frac{\Gamma_{\text{ann}}}{\Gamma_{\text{break}} + \Gamma_{\text{ann}}} \\ &= \left(1 + \frac{\langle \sigma v_{\text{rel}} \rangle_{\text{ann}}^{BS_i} m^3 e^{-zE_{BS_i}/m}}{2R_{BS}(2s+1)(4\pi z)^{3/2}\Gamma_i} \right)^{-1}, \end{aligned} \quad (6)$$

where Γ_i is the annihilation rate of BS_i , R_{BS} is the representation size of the bound state, and E_{BS_i} is the binding energy [39]. Note the absence of the degrees of freedom squared factor in the second term of Eq. (6) when compared to Ref. [39]. This is due to a difference in conventions. We choose not to average the annihilation cross sections over the DM degrees of freedom here and instead do so when we compute the contribution to the effective annihilation cross section (see Sec. V). However, in Ref. [39] the cross sections *are* averaged and this factor serves to undo this averaging to apply to bound states. The branching ratio interpolates smoothly between the regimes of complete breaking of bound states (at $T \gg E_{BS_i}$) and efficient decay of bound states (at $T \ll E_{BS_i}$).

Formation and breaking of bound states. Schematically, the relevant processes are



where $(XX)_{BS}$ denotes a colorless electroweak bound state with quantum numbers fixed by the gauge representation. At early times, the thermal bath of SM particles breaks the newly formed bound states on a timescale $\Gamma_{\text{break}}^{-1} \ll H^{-1}$, leading to detailed balance between formation and breaking: $n_{BS} \simeq n_{BS,\text{eq}}$, and thus negligible net depletion. As the temperature drops below the binding energy, $T \lesssim E_{BS}$, the breaking rate becomes Boltzmann suppressed, $\Gamma_{\text{break}} \propto e^{-E_{BS}/T}$, and bound states annihilate promptly with $\Gamma_{\text{ann}} \gg H$. In this limit the bound-state population does not accumulate and its effect can be incorporated through the effective rate in Eq. (5).

Thermal average of the bound state formation rate. For a potential induced by the exchange of an electroweak gauge boson of mass m_V , when $E_{BS} \gtrsim m_V$, the bound-state formation cross section is approximately (see Sec. VI)

$$\langle \sigma v_{\text{rel}} \rangle_{\text{form}}^{BS} \simeq \frac{2^9 \pi}{3} \frac{\alpha_{\text{eff}}}{m_X^2 v_{\text{rel}}} \frac{e^{-4\xi \arccot \xi}}{1 - e^{-2\pi\xi}}, \quad \xi = \frac{\alpha_{\text{eff}}}{v_{\text{rel}}}, \quad (8)$$

where α_{eff} is the coupling strength of the relevant potential. The thermally averaged rate $\langle \sigma v_{\text{rel}} \rangle_{\text{form}}^{BS}$ is then evaluated by integrating over the Maxwell–Boltzmann distribution of relative velocities. In the Coulombic regime, $\langle \sigma v_{\text{rel}} \rangle_{\text{form}}^{BS}$ scales approximately as

$$\langle \sigma v_{\text{rel}} \rangle_{\text{form}}^{BS} \simeq C_{BS} \frac{\alpha_{\text{eff}}^3}{m_X^2 \sqrt{z}}, \quad (9)$$

with C_{BS} a numerical factor of order unity that depends on the gauge representation and the available emission channels (γ , W or Z bosons, or Higgs).

Effect on the relic yield. When Eq. (4) is solved with the effective cross section of Eq. (5), the enhanced depletion through bound-state formation shifts the freezeout to larger values of z (lower temperatures) and reduces the final yield $Y_{DM}(\infty)$ relative to the standard case:

$$Y_{DM}(\infty) \simeq \frac{Y_{DM}^{\text{ann}}(\infty)}{1 + \Delta_{BS}}, \quad \Delta_{BS} \approx \frac{\sum_{BS_i} \langle \sigma v_{\text{rel}} \rangle_{\text{form}}^{BS_i}}{\langle \sigma v_{\text{rel}} \rangle_{\text{ann}}} \Big|_{z=z_f}. \quad (10)$$

For heavy electroweak multiplets, where $\alpha_{\text{eff}} m_X / m_V \gg 1$, the bound-state contribution is significant and must be included in determining the relic abundance and the corresponding unitarity limit on the thermal DM mass.

More quantitatively, Eq. (4) has the approximate asymptotic solution (see Ref. [39]),

$$Y_{DM}(\infty) = \frac{1}{\lambda} \left(\int_{z_f}^{\infty} \frac{\langle \sigma v_{\text{rel}} \rangle_{\text{eff}}(z)}{z^2} dz + \frac{\langle \sigma v_{\text{rel}} \rangle_{\text{eff}}(z_f)}{z_f^2} \right)^{-1}, \quad (11)$$

where $\lambda = \sqrt{g_{SM}\pi/45} M_{\text{Pl}} m$. z_f is given by

$$z_f = \ln \left(\frac{2(g_M + g_D) \langle \sigma v_{\text{rel}} \rangle_{\text{eff}}(z_f) \lambda}{(2\pi z_f)^{3/2}} \right). \quad (12)$$

In summary, the inclusion of electroweak bound-state formation and thermal breaking modifies the effective inelastic rate governing the chemical decoupling of heavy

DM. Equation (4) provides a compact formulation that self-consistently accounts for the transition from the regime ($T \gg E_{BS}$) to the annihilation-dominated regime ($T \ll E_{BS}$), thereby capturing the dominant impact of bound-state dynamics on the thermal freezeout of electroweak DM.

IV. POTENTIALS AND ANNIHILATION CROSS SECTIONS

In this section, we present the long-range potentials between DM particles that generate Sommerfeld corrections and bound states. We go on to discuss our formalism for handling the mixed $MM/D\bar{D}$ states that arise due to Higgs exchange (analogous to the mixing of the K^0 and \bar{K}^0 mesons arising from W^\pm exchange [52]). Finally, we show the annihilation cross sections to the SM for the various combinations of DM particles, with additional details in Appendix C.

A. Potentials

Figure 2 shows the diagrams arising from the Lagrangian in Eq. (3) that generate long-range potentials. Because we are considering heavy DM annihilation after $T \ll m$, we are interested in the non-relativistic limit of these processes.

We specify the kinematics with \vec{P} as the total momentum of the system and \vec{p} , \vec{k} as the momenta \vec{p}_1 , \vec{k}_1 in the center of momentum frame. Then

$$\vec{p}_1 = \frac{\vec{P}}{2} + \vec{p}, \quad \vec{p}_2 = \frac{\vec{P}}{2} - \vec{p}, \quad \vec{k}_1 = \frac{\vec{P}}{2} + \vec{k}, \quad \vec{k}_2 = \frac{\vec{P}}{2} - \vec{k}. \quad (13)$$

When considering long-range interactions, in the non-relativistic and $SU(2)_L$ symmetric ($m_H = m_W = m_B = 0$) limits, the amplitudes are

$$\begin{aligned} \mathcal{M}_{D\bar{D};MM} &= \frac{4m^2}{|\vec{p} - \vec{k}|^2} y_1 y_2 \\ \mathcal{M}_{D\bar{D}} &= \frac{4m^2}{|\vec{p} - \vec{k}|^2} (g_1^2 Y_D^2 - g_2^2 t_D^a t_{\bar{D}}^a) \\ \mathcal{M}_{DD} &= -\frac{4m^2}{|\vec{p} - \vec{k}|^2} (g_1^2 Y_D^2 + g_2^2 t_D^a t_{\bar{D}}^a) \\ \mathcal{M}_{MD} &= -\frac{4m^2}{|\vec{p} - \vec{k}|^2} (g_2^2 t_D^a t_M^a - y_1 y_2) \\ \mathcal{M}_{M\bar{D}} &= -\frac{4m^2}{|\vec{p} - \vec{k}|^2} (g_2^2 t_D^a t_M^a - y^2) \\ \mathcal{M}_{MM} &= -\frac{4m^2}{|\vec{p} - \vec{k}|^2} g_2^2 t_M^a t_M^a, \end{aligned} \quad (14)$$

where we have omitted the u -channel diagrams where they appear (see below).

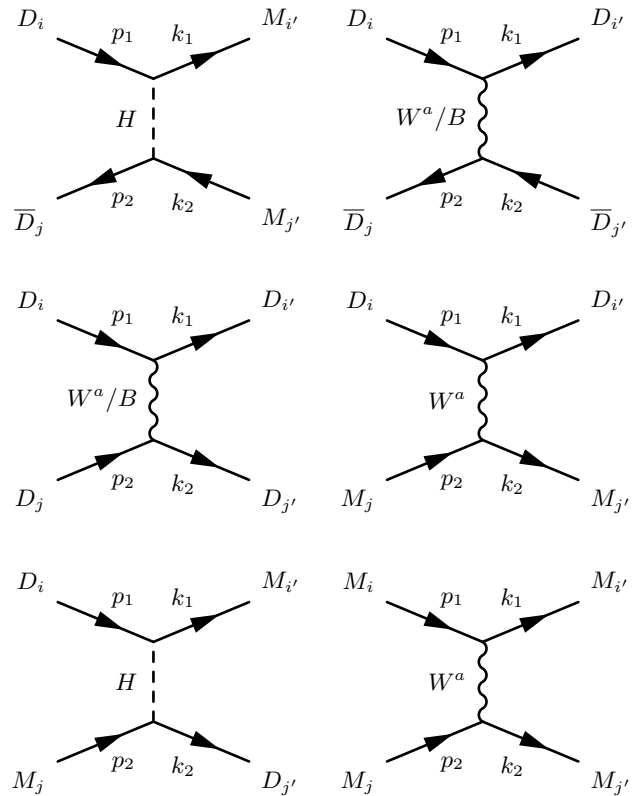


FIG. 2. Diagrams for the interactions generating long-range potentials among M and D . The spin indices are omitted because particle spins are individually conserved in the non-relativistic limit. The $M\bar{D}$ diagrams are omitted but follow straightforwardly from the MD cases.

Relating the scattering amplitude to the Born approximation, we find that the non-relativistic potential is

$$V = -\frac{1}{4m^2} \int \frac{d^3\vec{q}}{(2\pi)^3} \mathcal{M}(\vec{q}) e^{i\vec{q}\cdot\vec{r}}. \quad (15)$$

Note that for identical particles, we should in principle include u -channel diagrams. However, to obtain the correct non-relativistic, long-range potentials, we consider only the t -channel diagrams. This is analogous to what is commonly done to ensure that the non-relativistic, long-range Coulomb potential be same for e^-e^- (t - and u -channel diagrams) and $e^-\mu^-$ (t -channel diagram only) [53]. In short, the reasoning behind this is that the t -channel diagram generates the correct long-range $1/r$ potential in the Coulomb limit, while the u -channel diagram generates only short-range contact interactions, as we show below.

First we note that operationally, the effect of ignoring the u -channel diagrams is to consider that the particles are distinguishable. Arguments along these lines for the irrelevance of the u -channel diagrams in the long-range potential are given in Refs. [54, 55], which consider the particles distinguishable based on the wave-functions not overlapping significantly at long-range, and Ref. [56], which works in the context of the helium atom and finds that as the spatial separation between the two identi-

cal electrons grows the exchange interaction becomes increasingly infrequent.

To explicitly show that the t -channel diagrams generate long-range potentials while the u -channel diagrams only generate short-range potentials, we do the following. Working in the center-of-momentum frame, we define the momentum transfer used in the Born construction of the potential as

$$\vec{q} \equiv \vec{p} - \vec{k}, \quad (16)$$

where \vec{p} and \vec{k} are the initial and final relative momenta. For exchange of a mediator of mass m_V , the non-relativistic t -channel amplitude has the form

$$\mathcal{M}_t(\vec{q}) \propto \frac{g^2}{\vec{q}^2 + m_V^2}. \quad (17)$$

Using Eq. (15), this produces the familiar Yukawa potential,

$$V_t(r) \propto - \int \frac{d^3\vec{q}}{(2\pi)^3} \frac{e^{i\vec{q}\cdot\vec{r}}}{\vec{q}^2 + m_V^2} = -\frac{1}{4\pi r} e^{-m_V r}, \quad (18)$$

which reduces to the Coulomb form $V_t(r) \propto -1/r$ in the $SU(2)_L$ -symmetric limit.

For identical particles, the u -channel propagator depends instead on

$$\vec{q}_u = \vec{p} + \vec{k} = 2\vec{p} - \vec{q}, \quad (19)$$

so that

$$\mathcal{M}_u(\vec{q}) \propto \frac{g^2}{(2\vec{p} - \vec{q})^2 + m_V^2}. \quad (20)$$

In constructing the long-range potential, the Fourier transform is dominated by the region $|\vec{q}| \ll |\vec{p}|$. Expanding the propagator in this limit yields

$$\frac{1}{(2\vec{p} - \vec{q})^2 + m_V^2} = \frac{1}{4\vec{p}^2 + m_V^2} + \mathcal{O}\left(\frac{\vec{p} \cdot \vec{q}}{(4\vec{p}^2 + m_V^2)^2}\right), \quad (21)$$

so that, to leading order, the u -channel amplitude is independent of \vec{q} . Substituting into Eq. (15) gives

$$\begin{aligned} V_u(\vec{r}) &\propto -\frac{g^2}{4\vec{p}^2 + m_V^2} \int \frac{d^3\vec{q}}{(2\pi)^3} e^{i\vec{q}\cdot\vec{r}} \\ &= -\frac{g^2}{4\vec{p}^2 + m_V^2} \delta(\vec{r}), \end{aligned} \quad (22)$$

with higher-order terms producing derivatives of $\delta(\vec{r})$. The u -channel therefore generates only short-range contact interactions, while the long-range $1/r$ behavior arises solely from the t -channel exchange.

The neglect of u -channel diagrams in the derivation of the potential is thus equivalent to computing the long-range interaction in the distinguishable-particle approximation. The required antisymmetrization of identical-particle two-body states is imposed separately at the level

of the wavefunction and the bound-state formation amplitudes (see Sec. VI), ensuring that Pauli exclusion is fully respected while retaining the correct long-range potential governing Sommerfeld enhancement and bound-state formation.

In Eq. (14), the generator combinations can be simplified through the identity

$$\begin{aligned} t_{x_1}^a t_{x_2}^a &\rightarrow -\frac{1}{2}(C_2(R_{x_1}) + C_2(R_{x_2}) - C_2(R)) \\ &= C_R^{x_1 x_2}, \end{aligned} \quad (23)$$

where we have used R for the representation size of the combined state.

Therefore, the non-relativistic potentials are

$$\begin{aligned} V_{D\bar{D};MM} &= -\frac{\alpha_H}{r} \\ V_{D\bar{D}} &= -\frac{1}{r} \left(\frac{\alpha_1}{4} - \alpha_2 C_R^{D\bar{D}} \right) \\ V_{DD} &= \frac{1}{r} \left(\frac{\alpha_1}{4} + \alpha_2 C_R^{DD} \right) \\ V_{MD} &= \frac{1}{r} (\alpha_2 C_R^{MD} - \alpha_H) \\ V_{MM} &= \frac{\alpha_2 C_R^{MM}}{r}. \end{aligned} \quad (24)$$

In particular, the Yukawa potential $V_{D\bar{D};MM}$ contributions from scalar exchange is effectively $\propto y_1 y_2$ and is attractive when y_1, y_2 have the same sign as expected (see e.g., Ref. [53]). When these Yukawa couplings have opposite signs, the potential becomes repulsive and acquires an additional negative sign. In our analysis, this is the case when we consider large Yukawa couplings to evade direct-detection constraints (see the discussion in Sec. II). The α_H term in V_{MD} is also affected by this change, however $V_{M\bar{D}}$ is insensitive to it.

Furthermore, the V_{DD} and $V_{D\bar{D};MM}$ long-range potentials due to gauge boson exchange are always nonzero, independent of spin and angular momentum quantum numbers. Reference [36] obtained different results by considering the u -channel diagrams in their calculation of the potentials, which is only valid in the short-range limit. This is irrelevant to the formation of bound states which still obey Pauli exclusion from the selection rules in the bound-state formation cross sections (Sec. VI). However, the Sommerfeld corrections are affected.

B. Mixed states

Much of the methodology in this subsection is borrowed from Ref. [36], which considered the specific case of a Majorana singlet and Dirac doublet.

The first diagram in Fig. 2 allows for mixing between the MM and $D\bar{D}$ states. Because the representation must match on both sides, and

$$\begin{aligned} M \otimes M &= 1 \oplus \dots \oplus (2R_M - 1) \\ D \otimes \bar{D} &= 1 \oplus \dots \oplus (2R_D - 1), \end{aligned} \quad (25)$$

mixing can occur in the representations

$$R \leq \min\{2R_M - 1, 2R_D - 1\}. \quad (26)$$

We form the vector

$$\Phi(R) = \begin{pmatrix} \phi^{MM}(R) \\ \phi^{D\bar{D}}(R) \end{pmatrix}, \quad (27)$$

where $\phi^{X_1 X_2}$ are the two particle wavefunctions and we have omitted the \vec{r} dependence. This obeys the coupled Schrodinger equation

$$\left(-\frac{\nabla^2}{m} + \hat{V}^R\right) \Phi(R) = \mathcal{E}(R)\Phi(R), \quad (28)$$

where \hat{V}^R is the potential matrix

$$\hat{V}^R = -\frac{1}{r} \begin{pmatrix} \alpha_{MM}^R & \alpha_{D\bar{D};MM}^R \\ \alpha_{D\bar{D};MM}^R & \alpha_{D\bar{D}}^R \end{pmatrix}. \quad (29)$$

When $\alpha_H \ll \alpha_2, \alpha_1$,

$$\hat{V}^R \rightarrow -\frac{1}{r} \begin{pmatrix} \alpha_{MM}^R & 0 \\ 0 & \alpha_{D\bar{D}}^R \end{pmatrix}, \quad (30)$$

so there is no $MM \rightleftharpoons D\bar{D}$ mixing, as expected.

When α_H is large ($\alpha_H \sim \alpha_2$), we require opposite signs between y_1 and y_2 . This produces an additional factor of -1 in the $D\bar{D} \rightleftharpoons MM$ potential. We continue to call

$$V_{D\bar{D};MM}^R = -\frac{\alpha_H}{r} \quad (31)$$

and put the negative sign into the potential matrix

$$\hat{V}^R \rightarrow -\frac{1}{r} \begin{pmatrix} \alpha_{MM}^R & -\alpha_{D\bar{D};MM}^R \\ -\alpha_{D\bar{D};MM}^R & \alpha_{D\bar{D}}^R \end{pmatrix}. \quad (32)$$

This matrix has eigenvalues

$$\alpha_{\text{mix}1,2}^R = \frac{1}{2} \left(\alpha_{D\bar{D}}^R + \alpha_{MM}^R \mp \sqrt{(\alpha_{D\bar{D}}^R - \alpha_{MM}^R + 4(\alpha_{D\bar{D};MM}^R)^2)} \right) \quad (33)$$

and eigenvectors

$$\vec{E}_{\text{mix}1,2}^R = C_{\text{mix}1,2} \begin{pmatrix} -\frac{\alpha_{MM}^R - \alpha_{D\bar{D}}^R \mp \sqrt{(\alpha_{D\bar{D}}^R - \alpha_{MM}^R + 4(\alpha_{D\bar{D};MM}^R)^2)}}{2\alpha_{D\bar{D};MM}^R} \\ 1 \end{pmatrix}$$

$$C_{\text{mix}1,2} = \frac{1}{\sqrt{1 + \left(\frac{\alpha_{MM}^R - \alpha_{D\bar{D}}^R \mp \sqrt{(\alpha_{D\bar{D}}^R - \alpha_{MM}^R + 4(\alpha_{D\bar{D};MM}^R)^2)}}{2\alpha_{D\bar{D};MM}^R} \right)^2}} \quad (34)$$

where upper (lower) signs correspond to the mix1 (mix2) eigenstates.

We can use the matrix

$$\hat{P}^R = \begin{pmatrix} \vec{E}_{\text{mix}1}^R & \vec{E}_{\text{mix}2}^R \end{pmatrix} \quad (35)$$

to diagonalize \hat{V}^R

$$\begin{aligned} \tilde{V}^R &= \left(\hat{P}^R\right)^{-1} \hat{V}^R \hat{P}^R \\ &= -\frac{1}{r} \begin{pmatrix} \alpha_{\text{mix}1}^R & 0 \\ 0 & \alpha_{\text{mix}2}^R \end{pmatrix}. \end{aligned} \quad (36)$$

Then the vector

$$\begin{aligned} \tilde{\Phi}(R) &= \begin{pmatrix} \tilde{\phi}_1(R) \\ \tilde{\phi}_2(R) \end{pmatrix} = \begin{pmatrix} w_{\text{mix}1MM} \phi^{MM} + w_{\text{mix}1D\bar{D}} \phi^{D\bar{D}} \\ w_{\text{mix}2MM} \phi^{MM} + w_{\text{mix}2D\bar{D}} \phi^{D\bar{D}} \end{pmatrix} \\ &= \left(\hat{P}^R\right)^{-1} \Phi(R) \hat{P}^R \end{aligned} \quad (37)$$

obeys the uncoupled Schrodinger equation

$$\left(-\frac{\nabla^2}{m} + \tilde{V}^R\right) \tilde{\Phi}(R) = \mathcal{E}(R)\tilde{\Phi}(R). \quad (38)$$

The two states $\tilde{\phi}_{1,2}$ evolve in the potentials of magnitude $-\alpha_{\text{mix}1,2}/r$, respectively.

When we compute the Sommerfeld corrections and bound-state formation rates, we need to work in terms of definite potentials. Therefore, we use the $\tilde{\phi}$ states. We then project back onto the $\phi^{MM, D\bar{D}}$ states to calculate annihilation rates.

C. Annihilation cross sections

Here we compile the tree-level annihilation cross sections for M and D in the $SU(2)_L$ symmetric limit, which we apply later to the annihilation of scattering and bound states. We do not average over the initial degrees of freedom here because these are different between scattering and bound states.

For a single multiplet X , the tree-level annihilation is given in Ref. [12]:

$$\begin{aligned} (\sigma v_{\text{rel}})_{XX} &= \frac{1}{16m_X^2 g_X} (\pi \alpha_2^2 (2R_X^4 + 17R_X^2 - 19) \\ &\quad + 4Y_X^2 \alpha_1^2 (41 + 8Y_X^2) + 16\alpha_1 \alpha_2 Y_X^2 (R_X^2 - 1)). \end{aligned} \quad (39)$$

The contributions due to the hypercharge gauge boson, B , emission and mediation have factors of Y_X . For a Dirac fermion with $Y_X = 1/2$, we can compute the relative contribution of B processes to the total cross section. For a doublet,

$$\frac{(\sigma v_{\text{rel}})_{XX}^B}{(\sigma v_{\text{rel}})_{XX}^{\text{tot}}} \approx 0.08. \quad (40)$$

The relative contribution is small for the doublet and decreases with increasing multiplet size, so we neglect this contribution. This is straightforward to add back in if one wants increased accuracy for a specific model.

Additionally, we only consider processes with zero angular momentum ($\ell = 0$). Annihilation for $\ell > 0$ is suppressed by higher powers of α relative to $\ell = 0$, so their contribution is sub-dominant [29]. This is a conservative choice which underpredicts the overall annihilation cross section and therefore the mass.

For M, D in the in the non-relativistic limit, we have:

$$\begin{aligned}
{}^0(\sigma v_{\text{rel}})_{D\bar{D};WW}^{0,2} &= \frac{\pi\alpha_2^2}{m^2} (G_{D\bar{D};WW}^{ab} + G_{D\bar{D};WW}^{ba})^2 \\
{}^1(\sigma v_{\text{rel}})_{D\bar{D};HH^*}^{0,1} &= \frac{4\pi\alpha_H^2}{m^2} \\
{}^1(\sigma v_{\text{rel}})_{D\bar{D};f\bar{f}}^1 &= \frac{2\pi\alpha_2^2}{m^2} n_f G_{D\bar{D};f\bar{f}}^2 \\
{}^0(\sigma v_{\text{rel}})_{MM;WW}^{0,2} &= \frac{\pi\alpha_2^2}{2m^2} (G_{MM;WW}^{ab} + G_{MM;WW}^{ba})^2 \\
{}^1(\sigma v_{\text{rel}})_{MM;HH^*}^{0,1} &= \frac{8\pi\alpha_H^2}{m^2} \\
{}^1(\sigma v_{\text{rel}})_{MM;f\bar{f}}^1 &= \frac{\pi\alpha_2^2}{m^2} n_f G_{MM;f\bar{f}}^2 \\
{}^1(\sigma v_{\text{rel}})_{D\bar{D};HH}^{0,1} &= \frac{4\pi\alpha_H^2}{m^2} \\
{}^1(\sigma v_{\text{rel}})_{D\bar{D};H^*H^*}^{0,1} &= \frac{4\pi\alpha_H^2}{m^2} \\
{}^1(\sigma v_{\text{rel}})_{M\bar{D};WH}^{1/2,3/2} &= \frac{2\pi\alpha_H\alpha_2}{m^2} (\pm_1 G_{M\bar{D};WH} + \pm_2 G_{M\bar{D};WH})^2 \\
{}^1(\sigma v_{\text{rel}})_{M\bar{D};WH^*}^{1/2,3/2} &= \frac{2\pi\alpha_H\alpha_2}{m^2} (\pm_1 G_{M\bar{D};WH^*} + \pm_2 G_{M\bar{D};WH^*})^2
\end{aligned} \tag{41}$$

where the G terms are gauge factors that depend on Clebsch-Gordon coefficients (see Appendix C for details and derivations of the amplitudes). The cross sections for $MM/D\bar{D};HH^*$ specifically refer to the t -channel process. To account for $MM/D\bar{D} \rightarrow W \rightarrow HH^*$, we use the $MM/D\bar{D} \rightarrow W \rightarrow f\bar{f}$ cross sections, replacing $n_f = 12 \rightarrow n_p = 25/2$, where n_p is the number of SM fermions plus an additional 1/2 that arises from this process.

V. ANNIHILATION OF SCATTERING STATES

In this section, we discuss the direct annihilation process of two DM particles to SM particles (direct in that the annihilation proceeds without the formation of an intermediate bound state). We then detail how this will be applied to the effective cross section introduced in Sec. III.

For a two-particle process ($X_1 + X_2 \rightarrow X_3 + X_4$), the cross section is modified by the Sommerfeld factor:

$$\sigma v \rightarrow S\sigma v. \tag{42}$$

This factor accounts for the long-range interactions driven by the potentials listed in Eq. (24). In the $SU(2)_L$ symmetric limit with massless Higgs and vector bosons,

$$S = \frac{2\pi\alpha_{\text{eff}}/v_{\text{rel}}}{1 - e^{-2\pi\alpha_{\text{eff}}/v_{\text{rel}}}}, \tag{43}$$

where $p = mv_{\text{rel}}/2$.

We now apply the Sommerfeld corrections to the annihilation of scattering states. Because the Sommerfeld factor depends on α_{eff} , which itself depends on the particle combination and representation, we need to use the isospin decomposition of cross sections in Eq. (41). These cross sections also need to be averaged over the initial degrees of freedom. For scattering states, this gives a $(g_M + g_D)^2$ factor in the denominator. Therefore,

$$(\sigma v_{\text{rel}})_{\text{ann}} = \frac{2}{(g_M + g_D)^2} \sum_{j \geq i} \sum_i \sum_I \sum_{s=0,1} {}^s(S\sigma v_{\text{rel}})_{ij}^I, \tag{44}$$

where $i, j = 1, 2, 3$ correspond to M, D, \bar{D} and $I = 0, 1/2, 1, 3/2, 2$ to account for all possible SM final states. The factor of 2 arises in different ways for $i \neq j$ and $i = j$. When $i \neq j$, this accounts for the two possible ways to form a combination of distinguishable particles (see Ref. [57]). When $i = j$, this factor accounts for the two identical particles lost in the annihilation and effectively cancels a symmetry factor of 1/2 in the cross section (see Ref. [12] Sec. 4.1.3). In the latter case, this factor would be more logically included in the Boltzmann equation. However, because we obtain a common factor in both cases, we include it in the effective cross section for convenience. We use $(\sigma v_{\text{rel}})_{ij}$ to mean the cross section for annihilation of i, j to any SM final state.

When α_H is large, the MM and $D\bar{D}$ states do not have defined potentials due to mixing. Consequently, we exclude MM and $D\bar{D}$ states from Eq. (44) and instead include the terms ${}^s(S\sigma v_{\text{rel}})_{\text{mix}1,2}^I$. From Eq. (37), we see that

$$\begin{aligned}
{}^s(S\sigma v_{\text{rel}})_{\text{mix}1,2}^I &= \\
2 {}^s(S_{\text{mix}1,2}) & [w_{\text{mix}1,2MM}^2 (\sigma v_{\text{rel}})_{MM} + w_{\text{mix}1,2D\bar{D}}^2 (\sigma v_{\text{rel}})_{D\bar{D}}] \tag{45}
\end{aligned}$$

VI. FORMATION AND ANNIHILATION OF BOUND STATES

In this section, we calculate the cross sections for formation of DM bound states as well as their annihilation rate to the SM. We conclude with the implementation for the mixed $MM/D\bar{D}$ states.

As with the scattering state annihilation cross sections, we only consider bound states with $\ell = 0$. States with higher angular momentum annihilate inefficiently and generally break before annihilating. These states can transition to $\ell = 0$ and then annihilate, but we ignore this because it is subdominant. This is a conservative choice whose overall effect is to underestimate the DM mass necessary to reproduce the observed density.

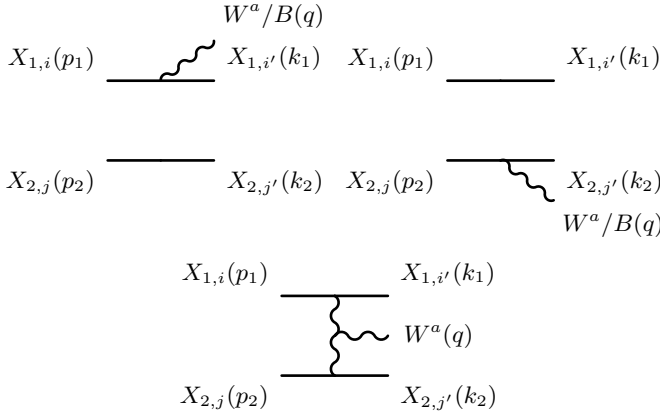


FIG. 3. Diagrams for bound-state formation through vector-boson emission. Mediators of the potential are not shown.

A. Formation

The amplitudes and overlap integrals used in this section, are derived in detail in Appendix D. We denote bound-state formation cross sections with a left subscript indicating the boson emitted (e.g., ${}^s_W(\sigma_{v_{\text{rel}}})_{X_1 X_2}^I$). The bound state also depends on the quantum numbers $n\ell m$, however these are suppressed in our notation.

We consider formation through emission of W , B and H bosons in Secs. VIA 1–VIA 3, respectively.

1. W emission

Figure 3 shows the processes $X_1 X_2 \rightarrow BS(X_1 X_2) + W$. Because W has spin one and the individual particle spins are conserved in the process, we must have $|\Delta\ell| = 1$ from the initial to bound state. In the center of momentum frame, we have

$$\sigma_{v_{\text{rel}}} = \frac{|\vec{q}|}{128\pi^2 m^3} \int d\Omega |\epsilon_\mu^{\alpha*}(q) \mathcal{M}^\mu|^2, \quad (46)$$

where q is the W^a 4-momentum, while \vec{q} denotes its 3-momentum, $\epsilon_\mu^a(q)$ is the polarization vector, and we have implicitly summed over the W boson polarizations. We temporarily omit all indices on the cross sections and restore them at the end.

In the massless W limit considered here, the sum over polarizations is $\sum_{\text{pol}} \epsilon_\nu^a \epsilon_\mu^{\alpha*} = -\eta_{\mu\nu}$. As in Ref. [29], we use the Ward identity, $q_\mu \mathcal{M}^\mu = 0$, to put the resulting expression entirely in terms of the spatial part of \mathcal{M}^μ , denoted with $\vec{\mathcal{M}}$,

$$\sigma_{v_{\text{rel}}} = \frac{|\vec{q}|}{128\pi^2 m^3} \int d\Omega \left(|\vec{\mathcal{M}}|^2 - \frac{|\vec{q} \cdot \vec{\mathcal{M}}|^2}{|\vec{q}|^2} \right). \quad (47)$$

Using $\vec{\mathcal{A}} = \vec{\mathcal{M}} / (8\sqrt{m}g_2)$, we perform the angular integral to get

$$\sigma_{v_{\text{rel}}} = \frac{8|\vec{q}|\alpha_2}{m^2} \frac{2}{3} |\vec{\mathcal{A}}|^2. \quad (48)$$

Because the gauge boson carries the binding energy,

$$|\vec{q}| \approx \frac{mv_{\text{rel}}^2}{2} \left(1 + \frac{\alpha_{BS}^2}{n^2 v_{\text{rel}}^2} \right). \quad (49)$$

The diagrams in Fig. 3 produce amplitudes with spatial parts of the form:

$$\begin{aligned} i\vec{\mathcal{A}} = & \frac{1}{2} \left((t_{X_1}^a)_{i'k} (\hat{\epsilon}_{X_1})_{ki} (\hat{\epsilon}_{X_2})_{j'j} - (t_{X_2}^a)_{j'k} (\hat{\epsilon}_{X_2})_{kj} (\hat{\epsilon}_{X_1})_{i'i} \right) \vec{J}^{ij, i'j'} \\ & - i (t_{X_1}^b)_{i'k} (\hat{\epsilon}_{X_1})_{ki} (t_{X_2}^c)_{j'l} (\hat{\epsilon}_{X_2})_{lj} f^{abc} \vec{T}^{ij, i'j'}, \end{aligned} \quad (50)$$

where \vec{J} , \vec{T} are overlap integrals that depend on p , $n\ell m$ (see Appendix D). We can decompose this into isospin channels and extract the $ij, i'j'$ dependence from the overlap integrals. Let

$$\begin{aligned} {}^W_J C_{X_1 X_2}^{IS, BS} = & \frac{1}{2} \left((t_{X_1}^a \hat{\epsilon}_{X_1})_{i'i} (\hat{\epsilon}_{X_2})_{j'j} - (\hat{\epsilon}_{X_1})_{i'i} (t_{X_2}^a \hat{\epsilon}_{X_2})_{j'j} \right) \\ & \langle I_{IS}, M_{IS} | I_{X_1}, I_{X_1}^3(i); I_{X_2}, I_{X_2}^3(j) \rangle \\ & \langle I_{BS}, M_{BS} | I_{X_1}, I_{X_1}^3(i'); I_{X_2}, I_{X_2}^3(j') \rangle \end{aligned} \quad (51)$$

and

$$\begin{aligned} {}^W_T C_{X_1 X_2}^{IS, BS} = & i f^{abc} (t_{X_1}^b \hat{\epsilon}_{X_1})_{i'i} (t_{X_2}^c \hat{\epsilon}_{X_2})_{j'j} \\ & \langle I_{IS}, M_{IS} | I_{X_1}, I_{X_1}^3(i); I_{X_2}, I_{X_2}^3(j) \rangle \\ & \langle I_{BS}, M_{BS} | I_{X_1}, I_{X_1}^3(i'); I_{X_2}, I_{X_2}^3(j') \rangle. \end{aligned} \quad (52)$$

Then

$$i\vec{\mathcal{A}} = {}^W_J C_{X_1 X_2}^{IS, BS} \vec{J} - {}^W_T C_{X_1 X_2}^{IS, BS} \vec{T}, \quad (53)$$

and the overlap integrals have no dependence on the $SU(2)_L$ indices. We have omitted the $M_{IS, BS}$ arguments of ${}^W_{J, T} C_{X_1 X_2}^{IS, BS}$, because these coefficients are contracted and summed over when $\vec{\mathcal{A}}$ is squared.

If $X_1 = X_2 = X$, we also have u -channel diagrams. These get a factor of -1 from fermion exchange as a well as a factor

$$(-1)^{\ell + s + 1 + 2I_X - I}, \quad (54)$$

where I refers to the isospin of the combined state, from the symmetries of the wavefunction. Note in particular that we have used the identity for CG coefficients

$$\langle J, M | j_1, m_1; j_2, m_2 \rangle = (-1)^{J - j_1 - j_2} \langle J, M | j_2, m_2; j_1, m_1 \rangle. \quad (55)$$

which gives rise to the power $2I_X - I$ in Eq. (54). Because $I_{BS} = I_{IS} \pm 1$, $\ell_{BS} = \ell_{IS} \pm 1$, and $s_{IS} = s_{BS}$, it does not matter whether we use the initial-state or bound-state quantum numbers, as long as we use choose one state consistently for all factors.

We also divide by a symmetry factor for the identical particles in the initial and final states. Therefore, we multiply the cross section by

$$\rho_{X_1 X_2} = \begin{cases} 1 & X_1 \neq X_2 \\ (1 - (-1)^{\ell+s+1+2I_X-I})^2 / 4 & X_1 = X_2. \end{cases} \quad (56)$$

Averaging over initial states and summing over spins, we obtain

$$\begin{aligned} {}^s(\sigma v_{\text{rel}})_{X_1 X_2}^{I_{IS} I_{BS}} &= \frac{2s+1}{(g_M + g_D)^2} \frac{8\alpha_2}{m^2} \frac{m v_{\text{rel}}^2}{2} \left(1 + \frac{\alpha_{BS}^2}{n^2 v_{\text{rel}}^2} \right) \\ &\quad \frac{2}{3} \rho_{X_1 X_2} \left| {}^W C_{X_1 X_2}^{I_{IS}, BS} \vec{J} - {}^W C_{X_1 X_2}^{I_{IS}, BS} \vec{T} \right|^2. \end{aligned} \quad (57)$$

If we explicitly evaluate the overlap integrals, we obtain the results of Ref. [29], as expected.

2. B emission

For B -emission, we only have the first two diagrams from Fig. 3. We can read off the cross section from the W -emission case. In Eq. (50) we replace

$$\begin{aligned} (t_{X_1}^a)_{i'k} (\hat{\epsilon}_{X_1})_{ki} (\hat{\epsilon}_{X_2})_{j'j} &\rightarrow Y_{X_1} (\hat{\epsilon}_{X_1})_{i'i} (\hat{\epsilon}_{X_2})_{j'j} \\ (t_{X_2}^a)_{j'k} (\hat{\epsilon}_{X_2})_{kj} (\hat{\epsilon}_{X_1})_{i'i} &\rightarrow Y_{X_2} (\hat{\epsilon}_{X_1})_{i'i} (\hat{\epsilon}_{X_2})_{j'j} \\ i(t_{X_1}^b)_{i'i} (t_{X_2}^c)_{j'j} f^{abc} \vec{T}^{ij, i'j'} &\rightarrow 0. \end{aligned} \quad (58)$$

We define

$$\begin{aligned} {}^B C_{X_1 X_2}^{I_{IS}, BS} &= \frac{1}{2} (Y_{X_1} - Y_{X_2}) (\hat{\epsilon}_{X_1})_{i'i} (\hat{\epsilon}_{X_2})_{j'j} \\ &\quad \langle I_{IS}, M_{IS} | I_{X_1}, I_{X_1}^3(i); I_{X_2}, I_{X_2}^3(j) \rangle \\ &\quad \langle I_{BS}, M_{BS} | I_{X_1}, I_{X_1}^3(i'); I_{X_2}, I_{X_2}^3(j') \rangle. \end{aligned} \quad (59)$$

When $X_1 = X_2$ this is zero, so we do not need to consider u -channel factors. After averaging over initial states and summing over spins, we get

$$\begin{aligned} {}^s(\sigma v_{\text{rel}})_{X_1 X_2}^I &= \frac{2s+1}{(g_M + g_D)^2} \frac{8\alpha_1}{m^2} \frac{m v_{\text{rel}}^2}{2} \left(1 + \frac{\alpha_{BS}^2}{n^2 v_{\text{rel}}^2} \right) \\ &\quad \frac{2}{3} \left| {}^B C_{X_1 X_2}^{I_{IS}, BS} \vec{J} \right|^2. \end{aligned} \quad (60)$$

3. H emission

Figures 4 and 5 show two examples in detail from which we can extract all of the H -emission bound-state formation cross sections.

MM bound states. MM bound-state formation with Higgs emission occurs through the two diagrams in Fig. 4. These diagrams do not interfere so we can compute the cross sections separately and add them together.

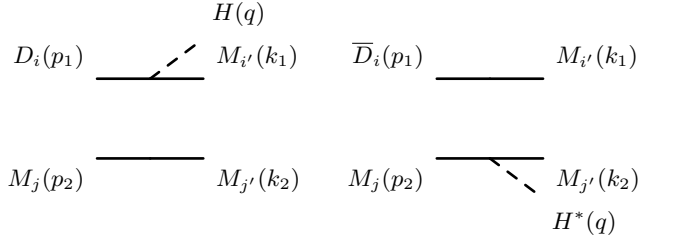


FIG. 4. Diagrams for MM bound-state formation through H emission. We follow the convention of Fig. 3 and omit the mediators of the potential.

The t -channel contribution to the first diagram for a given initial state produces the cross section (again suppressing indices on the cross section)

$$\begin{aligned} \sigma v_{\text{rel}} &= \frac{4\alpha_H}{m^2} \frac{m v_{\text{rel}}^2}{2} \left(1 + \frac{\alpha_{BS}^2}{n^2 v_{\text{rel}}^2} \right) \\ &\quad \left| (\hat{\epsilon}_D)_{ki} \delta_{I_D^3(k) \pm 1/2}^{I_M^3(i')} (\hat{\epsilon}_M)_{j'j} F^{ij, i'j'} \right|^2, \end{aligned} \quad (61)$$

where F is an overlap integral and we have divided by two for the identical final state particles. We define

$$\begin{aligned} {}^H C_{DM; MM}^{I_{IS}, BS} &= (\hat{\epsilon}_D)_{i'i} (\hat{\epsilon}_M)_{j'j} \langle I_{IS}, M_{IS} | I_D, I_D^3(i); I_M, I_M^3(j) \rangle \\ &\quad \langle I_{BS}, M_{BS} | I_M, I_D^3(i') \pm 1/2; I_M, I_M^3(j') \rangle \end{aligned} \quad (62)$$

which accounts for the contribution to the transition amplitude from each isospin channel. We also have a u -channel version of this diagram that receives the same factor as in the W -emission case. Putting these pieces together,

$$\begin{aligned} \sigma v_{\text{rel}} &= \frac{4\alpha_H}{m^2} \frac{m v_{\text{rel}}^2}{2} \left(1 + \frac{\alpha_{BS}^2}{n^2 v_{\text{rel}}^2} \right) (1 - (-1)^{\ell+s+1+2I_M-I_{BS}})^2 \\ &\quad \left| {}^H C_{DM; MM}^{I_{IS}, BS} \right|^2 |F|^2. \end{aligned} \quad (63)$$

The swap $D \rightarrow \bar{D}$ in the initial state only affects the calculation by changing the initial state potential in the large α_H case. So the second diagram cross section is given by Eq. (63) as well.

Adding the diagrams, averaging over initial states, and summing spins, we get the total H -emission cross section to form a MM bound state,

$$\begin{aligned} {}^s(\sigma v_{\text{rel}})_{MM}^I &= \frac{2s+1}{(g_M + g_D)^2} \frac{4\alpha_H}{m^2} \frac{m v_{\text{rel}}^2}{2} \left(1 + \frac{\alpha_{BS}^2}{n^2 v_{\text{rel}}^2} \right) \\ &\quad (1 - (-1)^{\ell+s+1+2I_M-I_{BS}})^2 \\ &\quad \left(\left| {}^H C_{DM; MM}^{I_{IS}, BS} \right|^2 |F|^2 + \left| {}^H C_{\bar{D}M; MM}^{I_{IS}, BS} \right|^2 |F|^2 \right). \end{aligned} \quad (64)$$

We have written F separately for each term because it depends on the initial state, which is different between the terms.

$M\bar{D}$ bound states. The diagrams in Fig. 5 show the processes for $M\bar{D}$ bound-state formation with H -emission. We note that the diagrams in the second row

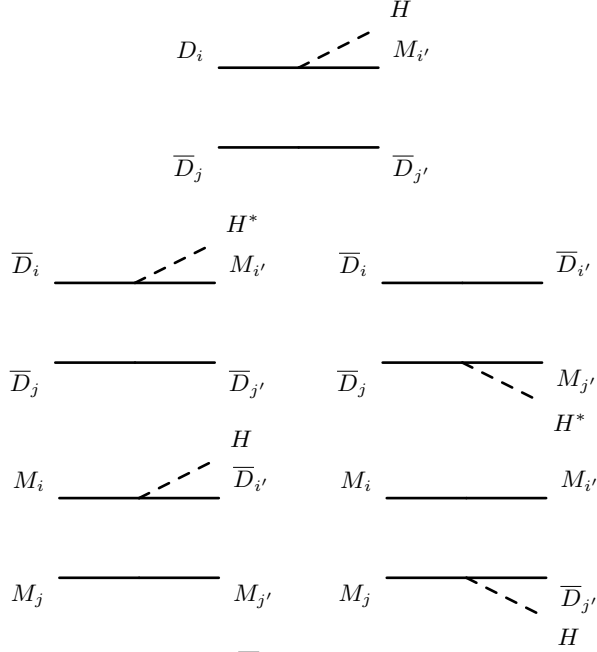


FIG. 5. Diagrams for $M\bar{D}$ bound-state formation through H emission. We follow the convention of Fig. 3 and omit the mediators of the potential.

do interfere and have u -channels, as do the diagrams in the third row.

The diagram in the first row can be read off directly from the MM case. We obtain Eq. (64) with the u -channel factor removed and ${}^H C_{DM;MM}^{IS,BS} \rightarrow {}^H C_{D\bar{D};M\bar{D}}^{IS,BS}$.

For the diagrams in the second row, temporarily suppressing indices on σv_{rel} , we get

$$\sigma v_{\text{rel}} = \frac{4\alpha_H}{m^2} \frac{mv_{\text{rel}}}{2} \left(1 + \frac{\alpha_{BS}^2}{v_{\text{rel}}^2 n^2} \right) \left| \left(\delta_{I_D^3(k)\pm 1/2}^{I_M^3(i')} (\hat{\epsilon}_D)_{ik} (\hat{\epsilon}_D)_{jj'} + \delta_{I_D^3(k)\pm 1/2}^{I_M^3(j')} (\hat{\epsilon}_D)_{jk} (\hat{\epsilon}_D)_{ii'} \right) F^{ij, i'j'} \right|^2. \quad (65)$$

Here we need to be careful with indices. We accomplish this by making the ordering of subscripts significant. By that we mean that we write the process $\bar{D}_i \bar{D}_j; M_{i'} \bar{D}_{j'}$ as $\bar{D}\bar{D}; M\bar{D}$ and $\bar{D}_i \bar{D}_j; \bar{D}_{i'} M_{j'}$ as $\bar{D}\bar{D}; \bar{D}M$, where the placement of each particle on each side of the semi-colon corresponds to its identity.

We again decompose the cross section into isospin channels by defining

$${}^H C_{\bar{D}\bar{D};M\bar{D}}^{IS,BS} = (\hat{\epsilon}_D)_{ii'} (\hat{\epsilon}_D)_{jj'} \langle I_{IS}, M_{IS} | I_D, I_D^3(i); I_D, I_D^3(j) \rangle \langle I_{BS}, M_{BS} | I_M, I_D^3(i') \pm 1/2; I_D, I_D^3(j') \rangle. \quad (66)$$

We see that

$${}^H C_{\bar{D}\bar{D};\bar{D}M}^{IS,BS} = {}^H C_{\bar{D}\bar{D};M\bar{D}}^{IS,BS} (-1)^{1+I_D+I_M-(I_{IS}+I_{BS})}. \quad (67)$$

where we have used the identity in Eq. (55). We can now

write the cross section as

$${}^s_H(\sigma v_{\text{rel}})_{\bar{D}\bar{D};M\bar{D}}^{IS,BS} = \frac{4\alpha_H}{m^2} \frac{mv_{\text{rel}}^2}{2} \left(1 + \frac{\alpha_{BS}^2}{v_{\text{rel}}^2 n^2} \right) \left| {}^H C_{\bar{D}\bar{D};M\bar{D}}^{IS,BS} \right|^2 |F|^2 (1 - (-1)^{\ell+s+1+2I_D-I_{IS}})^2 (1 - (-1)^{I_D+I_M-(I_{IS}+I_{BS})})^2, \quad (68)$$

which includes the u -channel factor. We note that ℓ, s do not change in the process so we do not need to specify whether they are taken in the initial state or bound state.

For the third row, a similar calculation gives

$${}^s_H(\sigma v_{\text{rel}})_{MM;M\bar{D}}^{IS,BS} = \frac{4\alpha_H}{m^2} \frac{mv_{\text{rel}}^2}{2} \left(1 + \frac{\alpha_{BS}^2}{v_{\text{rel}}^2 n^2} \right) \left| {}^H C_{MM;M\bar{D}}^{IS,BS} \right|^2 |F|^2 (1 - (-1)^{\ell+s+1+2I_M-I_{IS}})^2 (1 + (-1)^{I_D+I_M-(I_{IS}+I_{BS})})^2. \quad (69)$$

Therefore, the total cross section to form a $M\bar{D}$ bound state through H emission is

$${}^s_H(\sigma v_{\text{rel}})_{M\bar{D}}^{IS,BS} = \frac{2s+1}{(g_M+g_D)^2} \frac{8\alpha_H}{m^2} \frac{mv_{\text{rel}}^2}{2} \left(1 + \frac{\alpha_{BS}^2}{v_{\text{rel}}^2 n^2} \right) \left(\left| {}^H C_{\bar{D}\bar{D};M\bar{D}}^{IS,BS} \right|^2 |F|^2 + \frac{(1 - (-1)^{\ell+s+1+2I_D-I_{IS}})^2}{2} (1 + (-1)^{I_M+I_D-(I_{IS}+I_{BS})})^2 \left| {}^H C_{\bar{D}\bar{D};M\bar{D}}^{IS,BS} \right|^2 |F|^2 + \frac{(1 - (-1)^{\ell+s+1+2I_M-I_{IS}})^2}{2} (1 - (-1)^{I_M+I_D-(I_{IS}+I_{BS})})^2 \left| {}^H C_{MM;M\bar{D}}^{IS,BS} \right|^2 |F|^2 \right). \quad (70)$$

We again write F separately for each term because it depends on the initial states.

From these two examples, we can now compile all of the H emission BS formation cross sections. Let

$$A = \frac{2s+1}{(g_M+g_D)^2} \frac{4\alpha_H}{m^2} \frac{mv_{\text{rel}}^2}{2} \left(1 + \frac{\alpha_{BS}^2}{v_{\text{rel}}^2 n^2} \right). \quad (71)$$

Then

$$\begin{aligned} {}^s_H(\sigma v_{\text{rel}})_{MM}^{IS,BS} &= A(1 + (-1)^{\ell+s+2I_M-I_{BS}})^2 \left(\left| {}^H C_{DM;MM}^{IS,BS} \right|^2 |F|^2 + \left| {}^H C_{\bar{D}M;MM}^{IS,BS} \right|^2 |F|^2 \right) \\ {}^s_H(\sigma v_{\text{rel}})_{DD}^{IS,BS} &= A(1 + (-1)^{\ell+s+2I_D-I_{BS}})^2 \left| {}^H C_{MD;DD}^{IS,BS} \right|^2 |F|^2 \\ {}^s_H(\sigma v_{\text{rel}})_{\bar{D}\bar{D}}^{IS,BS} &= A(1 + (-1)^{\ell+s+2I_D-I_{BS}})^2 \left| {}^H C_{M\bar{D};\bar{D}\bar{D}}^{IS,BS} \right|^2 |F|^2 \\ {}^s_H(\sigma v_{\text{rel}})_{D\bar{D}}^{IS,BS} &= A \left(\left| {}^H C_{MD;D\bar{D}}^{IS,BS} \right|^2 |F|^2 + \left| {}^H C_{M\bar{D};D\bar{D}}^{IS,BS} \right|^2 |F|^2 \right) \\ {}^s_H(\sigma v_{\text{rel}})_{M\bar{D}}^{IS,BS} &= \text{Eq. (70)} \\ {}^s_H(\sigma v_{\text{rel}})_{M\bar{D}}^{IS,BS} &= \text{Eq. (70)}. \end{aligned} \quad (72)$$

B. Annihilation rates

The annihilation rate for a bound state BS_i is given by

$$\Gamma_i = |\psi(0)|^2 (\sigma v_{\text{rel}})_{\text{ann}}^{BS_i}, \quad (73)$$

where $\psi(0)$ is the BS wavefunction evaluated at $r = 0$ and $(\sigma v_{\text{rel}})_{\text{ann}}^{BS_i}$ is the annihilation cross section of BS_i averaged over the bound state degrees of freedom. The radial part of the bound state wavefunction in the $SU(2)_L$ symmetric limit with massless vector and Higgs bosons is given by

$$R_{n\ell} = \left(\frac{\alpha_{\text{eff}} m}{n}\right)^{3/2} \sqrt{\frac{(n-\ell-1)!}{2n(n+\ell)!}} e^{-r\alpha_{\text{eff}} m/2n} \left(\frac{r\alpha_{\text{eff}}}{n}\right)^\ell L_{n-\ell-1}^{2\ell+1} \left(\frac{r\alpha_{\text{eff}} m}{n}\right), \quad (74)$$

where L are the Laguerre polynomials [29]. Therefore,

$$|\psi(0)|^2 = \frac{m^3 \alpha_{BS}^3}{2^3 \pi n^3}. \quad (75)$$

This annihilation rate is then used to determine the branching ratio as described in Sec. III.

The contribution to the effective annihilation cross section is then

$$\sum_{BS_i} \langle \sigma v_{\text{rel}} \rangle_{\text{form}}^{BS_i} BR(BS_i; SM), \quad (76)$$

where $(\sigma v_{\text{rel}})_{\text{form}}^{BS_i}$ is the total formation cross section of BS_i . When the bound state consists of identical particles, $BR(BS_i; SM)$ receives an additional factor of 2 to account for the disappearance of two particles of the same type in the annihilation because we have chosen not to include this in the Boltzmann equation (as described in Sec. V).

C. Bound $D\bar{D}/MM$ states

When we work with mixed $MM \rightleftharpoons D\bar{D}$ states, we project onto the $MM, D\bar{D}$ states to find the formation cross section

$$(\sigma v_{\text{rel}})_{\text{form}}^{\text{mix}1,2} = w_{\text{mix}1,2MM}^2 (\sigma v_{\text{rel}})_{\text{form}}^{MM} + w_{\text{mix}1,2D\bar{D}}^2 (\sigma v_{\text{rel}})_{\text{form}}^{D\bar{D}}. \quad (77)$$

Here we suppress the spin and isospin dependence. We then thermally average this cross section and project again to find the contribution to the effective cross section

$$\langle \sigma v_{\text{rel}} \rangle_{\text{form}}^{\text{mix}1,2} \left(w_{\text{mix}1,2MM}^2 BR(MM \rightarrow SM) + w_{\text{mix}1,2D\bar{D}}^2 BR(D\bar{D} \rightarrow SM) \right). \quad (78)$$

VII. RESULTS

In this section, we apply our formalism to determine the DM mass necessary for a viable HC-MDM model. We consider the $3M2D$, $5M4D$, $7M6D$, $9M8D$, $11M10D$, and $13M12D$ representations and match the relic abundance to the

observed DM mass density. We then use these results to determine the direct-detection prospects of HC-MDM. Finally, we discuss additional constraints on the Higgs coupling imposed by the unitarity bound.

A. Methodology

When the couplings $y_{1,2}$ are large, we have constrained them to have identical magnitudes (y) and opposite signs. However, these constants can take a continuum of values up to the limit of perturbativity. Therefore, to demonstrate their effect on the DM mass, we choose three values of y covering a range of scenarios and determine the mass of the DM particles in each case. We consider a small coupling ($y_{\text{small}} = 10^{-9}$), a mid-range coupling ($y_{\text{mid}} = 0.005$), and a large coupling ($y_{\text{large}} = 1$).

From the dependence of the branching ratio for bound states to the SM on the binding energy (see Eq. (6)), we see that we only need to consider the most deeply bound states for a given Majorana-Dirac multiplet combination. We determine the most deeply bound state for a particular combination, then (somewhat arbitrarily) consider any bound states with binding energy greater than a quarter of this value. Consideration of less deeply bound states is relatively straightforward, however the calculational expense quickly becomes overwhelming, especially for larger multiplets.

Our choice to only consider states with $E_{BS} > E_{BS,\text{max}}/4$ excludes states with $n > 1$, so all states within our consideration are manifestly $\ell = 0$ states. If one includes less deeply bound states, then it becomes necessary to consider states with non-zero angular momentum. As mentioned in Sec. VI, states with $|\ell| > 0$ annihilate inefficiently and generally break in the thermal bath or decay to $\ell = 0$ states then annihilate. The latter is subdominant to the direct formation and annihilation of $\ell = 0$ states (see Ref. [29]). Consideration of these states is beyond the scope of this work.

Similarly, bound states of representation size greater than five cannot annihilate directly to the standard model. Instead, these states can decay to lower representations through gauge boson emission, then annihilate to the SM. However, this is again a subdominant effect (considering that these states are necessarily not the most deeply bound states, see Eqs. (23) and (24)) and is ignored here.

We also need to consider the maximum value of z that we integrate Eq. (11) over to find the relic abundance. Because we are working in the $SU(2)_L$ symmetric limit and a component-wise calculation valid after symmetry breaking is beyond the scope of this work, the obvious answer is to integrate up to $z_{\text{sym}} = m/T_{\text{sym}}$, where the subscript ‘‘sym’’ denotes the temperature of symmetry breaking. This choice would greatly underestimate the DM mass because it would ignore a sizeable amount of annihilation after symmetry breaking. However, as noted in Ref. [29], the $SU(2)_L$ symmetric approx-

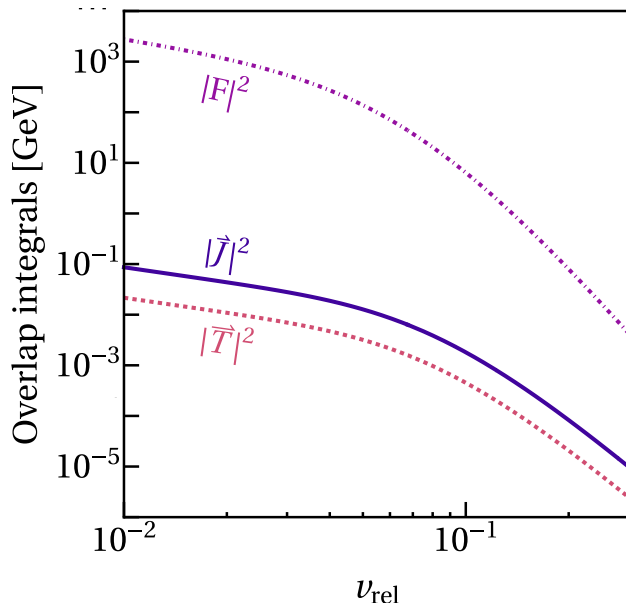


FIG. 6. Comparison of the overlap integral squared norms. All values taken with $m = 50$ TeV, $\alpha_{IS} = \alpha_2$, and $\alpha_{BS} = 2\alpha_2$.

imation remains approximately valid up $T_{\Delta m} \approx \Delta m \approx \alpha_{em} M_W$, where Δm is the mass splitting between members of the $SU(2)_L$ multiplet after symmetry breaking (see Ref. [13]). So we take as the upper limit of integration $z_{\Delta m} = m/0.58$ GeV. This still ignores some amount of annihilation taking place after the temperature decreases below the mass splitting, and a component-wise calculation becomes necessary for increased accuracy.

The effect of these choices is to mildly underestimate the overall annihilation cross section and, consequently, the DM mass. A more detailed treatment that avoids these simplifications may be justified for cases of particular interest.

Figure 6 shows the squared norms of the overlap integrals \vec{J} , \vec{T} , and F as functions of v_{rel} with arbitrary (but reasonable) choices of $m = 50$ TeV, $\alpha_{IS} = \alpha_2$, and $\alpha_{BS} = 2\alpha_2$ to compare their magnitudes. These significantly affect the W, B, H emission bound state formation amplitudes (see Eqs. (57, 60, 72)). We see that for values of α_H comparable to $\alpha_2 = 1/29.6$ (taken at the Z -boson mass scale for simplicity), the Higgs emission cross sections completely dominate the bound state formation. This is also the motivation behind our choice for y_{mid} . This value gives $\alpha_H |F|^2 \sim \alpha_2 |\vec{J}|^2$, so W and H emission cross sections are similar.

B. Small α_H

Table I shows the relevant bound states meeting the criteria described above for the y_{small} case. As noted in Sec. IV B, for small values of y , the mixed states $MM \rightleftharpoons D\bar{D}$ are essentially pure MM and $D\bar{D}$, so we can work in this basis. We make the additional distinc-

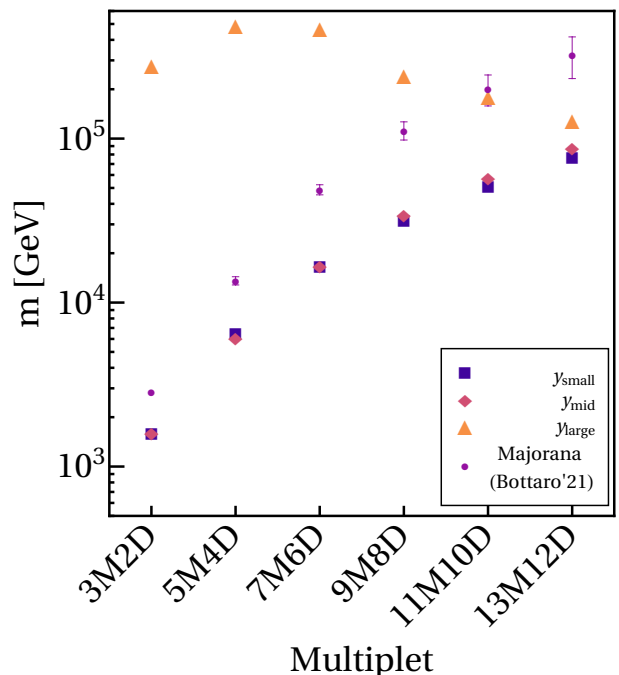


FIG. 7. DM mass needed to match the observed DM density to the computed relic abundance with y_{small} , y_{mid} , and y_{large} . Also shown are the corresponding pure Majorana states from Ref. [30]. Our values for the pure Majorana case are discussed in Appendix A.

tion that states which cannot annihilate efficiently are excluded. For example, the MD doublet has a binding energy above the threshold for the 5M4D and larger multiplets, however, this state cannot efficiently annihilate due to the smallness of α_H (see the cross sections in Eq. (41)), so it is not included.

Figure 7 shows the DM mass necessary to match the observed DM density to the computed relic abundance for the 3M2D, 5M4D, 7M6D, 9M8D, 11M10D, and 13M12D combinations as well as the pure Majorana case corresponding to each pair. In all cases, we find that the DM mass for the mixed multiplet case is less than the pure Majorana case. In this situation, the Higgs coupling has a negligible effect on the long-range potentials. Furthermore, annihilation into the Higgs is negligible, so

3M2D	5M4D	7M6D	9M8D	11M10D
MM^1	MM^1	MM^1	MM^1	MM^1
MM^3	MM^3	MM^3	MM^3	MM^3
	$D\bar{D}^1$	MM^5	MM^5	MM^5
		$D\bar{D}^1$	$D\bar{D}^1$	$D\bar{D}^1$
		$D\bar{D}^3$	$D\bar{D}^3$	$D\bar{D}^3$
		$D\bar{D}^5$	$D\bar{D}^5$	$D\bar{D}^5$

TABLE I. Bound states above the E_{BS} consideration threshold for $y_{small} = 10^{-9}$. Superscripts denote representation size. States are organized from largest to smallest binding energy. All states are $n = 1$, $\ell = 0$.

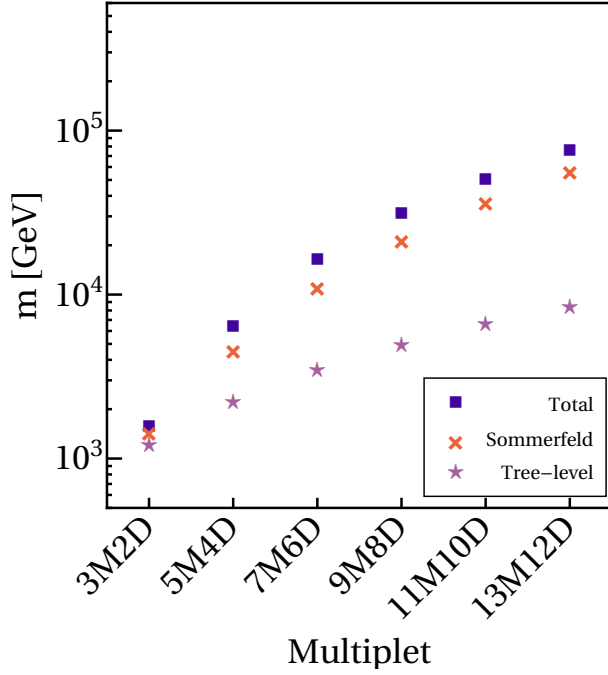


FIG. 8. Comparison of DM masses obtained from the tree-level, Sommerfeld enhanced, and total (including bound state effects) annihilation cross sections for y_{small} .

the only particle pairs that can efficiently annihilate are MM and DD . This means that only a fraction of the potential interacting pairs can annihilate, so this result matches our intuitive expectation. The exact value of the difference between the pure Majorana case and the mixed case is determined by this effect as well as the different potentials experienced by the MM and DD pairs.

Figure 8 compares the masses obtained from the tree-level, Sommerfeld enhanced, and total annihilation cross sections. For the $3M2D$ case, we see that the contribution from bound states is subdominant to the Sommerfeld enhancement. This matches the conclusion in Ref. [29] that for the pure Majorana triplet bound-state formation is less important than Sommerfeld enhancement. For the other multiplets, we see that the two effects are roughly comparable. In greater detail, we see that the relative importance of bound states grows from the $3M2D$, $5M4D$, and $7M6D$ cases and is then essentially constant for larger multiplets. This is influenced by our truncation of which bound states we calculate. A full accounting for all bound states would likely show a monotonically growing bound state contribution with multiplet size.

C. Mid α_H

Table II lists the bound states relevant for the y_{mid} case. Because y is no longer negligible, we now work in terms of the mixed $MM \rightleftharpoons DD$ states. For y_{mid} these states are still essentially pure MM and DD states (as can be

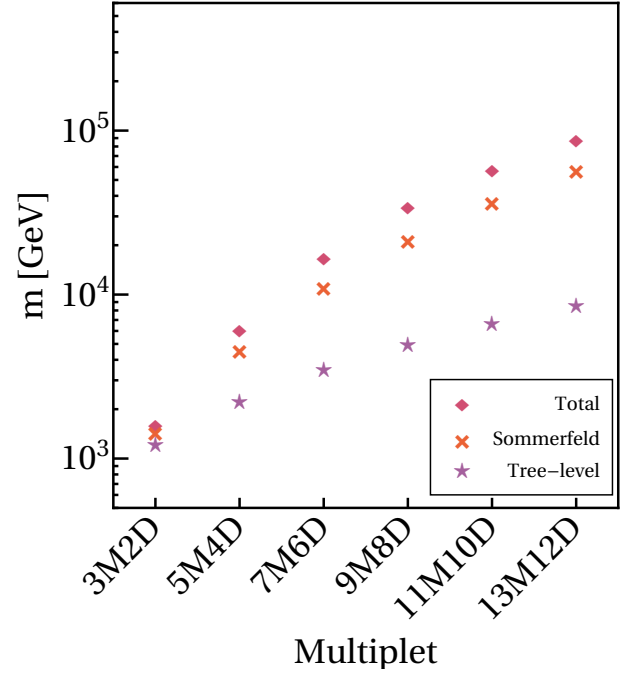


FIG. 9. Comparison of DM masses obtained from the tree-level, Sommerfeld enhanced, and total (including bound state effects) annihilation cross sections for y_{mid} .

confirmed from Eqs. (33), (35), and (37)), but working in this basis allows us to compare our results to the y_{large} case where these states are no longer approximated by the pure case.

Figure 7 compares the DM mass for the y_{mid} and the y_{small} cases. We find that for small multiplets the masses are approximately equal but slightly smaller for y_{mid} , while for larger representations the masses are larger for the y_{mid} condition. In all cases the mass remains lower than the pure Majorana case. This is again a result of

3M2D	5M4D	7M6D	9M8D	11M10D
mix2 ¹				
$M\bar{D}^2$	mix2 ³	mix2 ³	mix2 ³	mix2 ³
mix2 ³	$M\bar{D}^2$	$M\bar{D}^2$	$M\bar{D}^2$	$M\bar{D}^2$
	MD^2	MD^2	MD^2	mix2 ⁵
	mix1 ¹	mix2 ⁵	mix2 ⁵	MD^2
	$M\bar{D}^4$	mix1 ¹	$M\bar{D}^4$	$M\bar{D}^4$
		DD^1	MD^4	MD^4
		$M\bar{D}^4$	mix1 ¹	mix1 ¹
		MD^4	DD^1	DD^1
		mix1 ³	mix1 ³	mix1 ³
		DD^3	DD^3	DD^3
		mix1 ⁵	mix1 ⁵	mix1 ⁵

TABLE II. Bound states above the consideration threshold for Higgs coupling $y_{\text{mid}} = 0.005$. Superscripts denote representation size. States are organized from largest to smallest binding energy. All states are $n = 1$, $\ell = 0$.

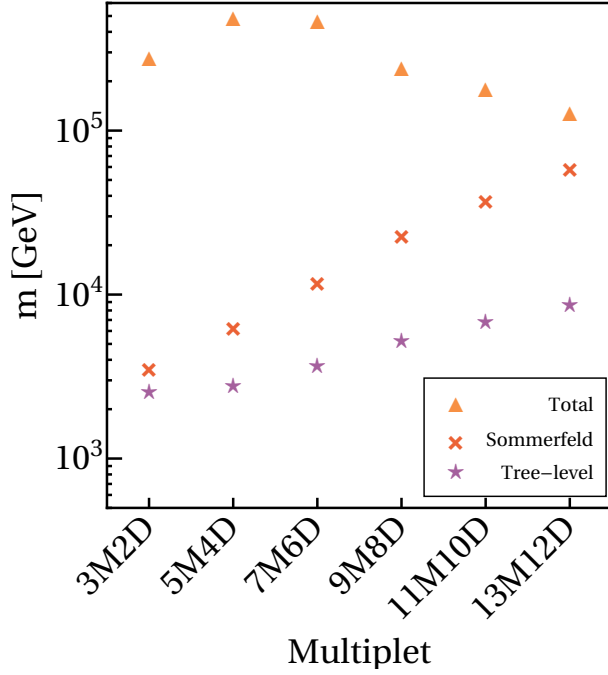


FIG. 10. Comparison of DM masses obtained from the tree-level, Sommerfeld enhanced, and (including bound state effects) annihilation cross sections for y_{large} .

the fact that no new annihilation channels are effectively open (because α_H is not multiplied by the overlap integral for the annihilation cross sections and $\alpha_H \ll \alpha_2$). However, for bound-state formation α_H appears in conjunction with $|F|^2$ so the combination is comparable to $\alpha_2 |\vec{J}|^2$ and bound-state formation is enhanced.

Figure 9 compares the masses obtained from the tree-level, Sommerfeld enhanced, and total annihilation cross sections, providing additional insight. We again see that for the $3M2D$ case the contribution from bound states is subdominant to the Sommerfeld enhancement. However, in this case we see that the relative importance of the bound contribution grows monotonically with increasing multiplet size. This effect would be even more pronounced without the bound state truncation used here.

D. Large α_H

Table III shows the y_{large} bound states. The separation between the MD and $M\bar{D}$ potentials for a given representation is larger than in the y_{mid} case. This is due to the relative sign change between y_1 and y_2 , which affects these two potentials differently, and the magnitude of y_{large} (see Sec. IV A).

Figure 7 shows that the Higgs coupling now has a large effect on the DM mass for smaller representation sizes compared to the pure Majorana case. For larger representations this effect diminishes and by the $11M10D$ case the mass is actually slightly smaller than for the pure Majorana.

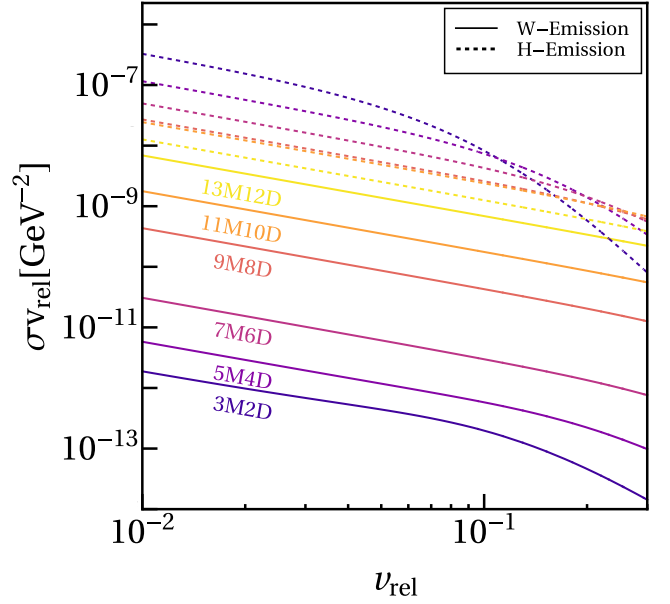


FIG. 11. bound-state formation cross sections through W (solid lines) and H (dashed lines) emission for y_{large} .

Figure 10 shows the origin of this behavior. First, bound state formation dominates the total cross section for all of the representations considered here. However, we see that the relative importance of bound states actually decreases for larger multiplet combinations.

Figure 11 shows the behavior of the bound state formation cross sections as a function of the relative velocity in detail. We see that the W -emission bound state formation cross sections grow monotonically with increasing multiplet size over the relevant velocity range as expected from the pure Majorana case (B -emission not shown because it is subdominant to W -emission and follows the same pattern). However, the H -emission cross section

3M2D	5M4D	7M6D	9M8D	11M10D
mix2 ¹				
$M\bar{D}^2$	$M\bar{D}^2$	$M\bar{D}^2$	mix2 ³	mix2 ³
mix2 ³	mix2 ³	mix2 ³	$M\bar{D}^2$	$M\bar{D}^2$
	$M\bar{D}^4$	$M\bar{D}^4$	$M\bar{D}^4$	mix2 ⁵
	mix2 ⁵	mix2 ⁵	mix2 ⁵	$M\bar{D}^4$
		DD^1	DD^1	DD^1
		DD^3	MD^2	MD^2
		MD^2	mix1 ¹	mix1 ¹
		mix1 ¹	DD^3	DD^3
			mix1 ³	MD^4
			MD^4	mix1 ³
			mix1 ⁵	mix1 ⁵

TABLE III. Bound states above the consideration threshold for $y_{\text{large}} = 1$. Superscripts denote representation size. States are organized from largest to smallest binding energy. All states are $n = 1, \ell = 0$.

actually decreases with the multiplet size, at least for $v_{rel} < 0.1$. We also see that for small multiplets the H -emission completely dominates the bound state formation cross section. However, due to the behavior noted above, this becomes much less pronounced for large multiplet combinations. Therefore, we find that the cross sections, and consequently the masses, begin to approach that of the small α_H case as the multiplet sizes increase. This is exactly what we see in Fig. 7.

E. Overall results

Our choices for y span the parameter space from an essentially negligible Higgs coupling to the perturbative limit. Because we have constrained $|y_1| = |y_2|$ and $y_{1,2}$ to have opposite signs in the large coupling case, the spin-independent cross section with nucleons is unchanged from the corresponding pure Majorana case for any mixed multiplet (see Ref. [35]). For small y , $y_{1,2}$ are the same sign but the coupling is negligible, so this statement remains true.

Figure 12 shows the possible masses for the $3M2D$, $5M4D$, $7M6D$, $9M8D$, $11M10D$, and $13M12D$ cases and their corresponding spin-independent (SI) cross sections on nuclei. The SI cross sections are taken from Ref. [30], which determined the cross-sections and their uncertainties in the pure Majorana case using lattice QCD calculations. Because we are considering $y_1 = -y_2$ and $m_D = m_M$, the tree-level Higgs mediated contribution to the cross section cancels and we can apply these to HC-MDM [35]. The validity of this cancellation when loop corrections are taken into account is discussed in Sec. VIII.

Figure 12 also shows the current exclusion limit from PandaX as well as the proposed sensitivity of XLZD [32]. We see that for the $3M2D$, $5M4D$, and $7M6D$ cases, significant portions of the parameter space lie below the neutrino floor. Therefore, we conclude that for lower multiplet mixtures, HC-MDM cannot be excluded by standard direct-detection efforts. Furthermore, we see that larger multiplet combinations lie entirely in the sensitivity range of the next generation of direct-detection experiments. Finally, we note again that we have repeatedly made conservative choices that underpredict the mass of the DM particles, so the parameter space will extend *further* below the neutrino floor in a more detailed calculation.

F. Comment on unitarity

Previously, we used an upper limit on y based on perturbativity. However, we can also impose the constraint that the s -wave processes considered here remain under the unitarity bound. When we only consider the s -wave,

we obtain the limit

$$(\sigma v)_{\text{ini}} \leq \frac{4\pi}{vm^2}, \quad (79)$$

where $(\sigma v)_{\text{ini}}$ refers to the cross section for an initial state (MM , DD , etc...) to annihilate or form a bound state (which might not match the initial state). This term is given schematically by

$$(\sigma v)_{x_1 x_2} = \frac{1}{g_{x_1} g_{x_2}} \left(\sum (\text{spin } 0) + \frac{1}{9} \sum (\text{spin } 1) \right), \quad (80)$$

where the two summations include the cross sections for $X_1 X_2 \rightarrow \text{SM}$ or BS in the relevant spin state. Note that since we have only considered bound states with $\ell = 0$ and $|\Delta\ell| = 1$ for W/B -emission, this only includes bound states formed through H -emission.

We note some subtleties unique to our choices in this paper when we do this computation. The cross-section in Eq. (44) should be divided by two when $i = j$. Furthermore, our expressions for the bound-state formation cross sections include an averaging over all possible DM initial states (see Eqs. (57), (60) and (72)). Consequently, these must be multiplied by $(g_M + g_D)^2$ so that this average can be replaced by the average over the relevant initial state as shown in Eq. (80).

Figure 12 shows the results of this calculation. The red shaded regions of the $3M2D$, $5M4D$, $7M6D$ parameter spaces indicate violation of s -wave unitarity. For the larger multiplets, unitarity is not violated up to our previously imposed limit of $y = 1$. In the three cases where unitarity is violated, we find that significant portions of the allowed parameter space still extend below the neutrino floor.

VIII. CONCLUSIONS

Due to its simplicity and predictive power, the minimal DM model is an especially compelling resolution to the particle nature of DM. For individual multiplets, this model is within the reach of the next generation of direct-detection experiments to be either confirmed or ruled out. But the answer has been unknown for a modest and important extension of this model, introducing two multiplets coupled by Higgs interactions.

In this paper, we have presented a detailed framework for calculating the relic abundance for HC-MDM. This includes both the tree-level annihilation cross section as well as the enhancement from Sommerfeld effects and bound-state formation. Furthermore, this formalism can be used with slight modification (mainly setting a series of parameters to zero) in individual-multiplet MDM models. We then use this formalism to determine the relic abundance of various viable multiplet combinations. Assuming that a given combination makes up the entirety of DM, we also determine the mass required for each multiplet combination.

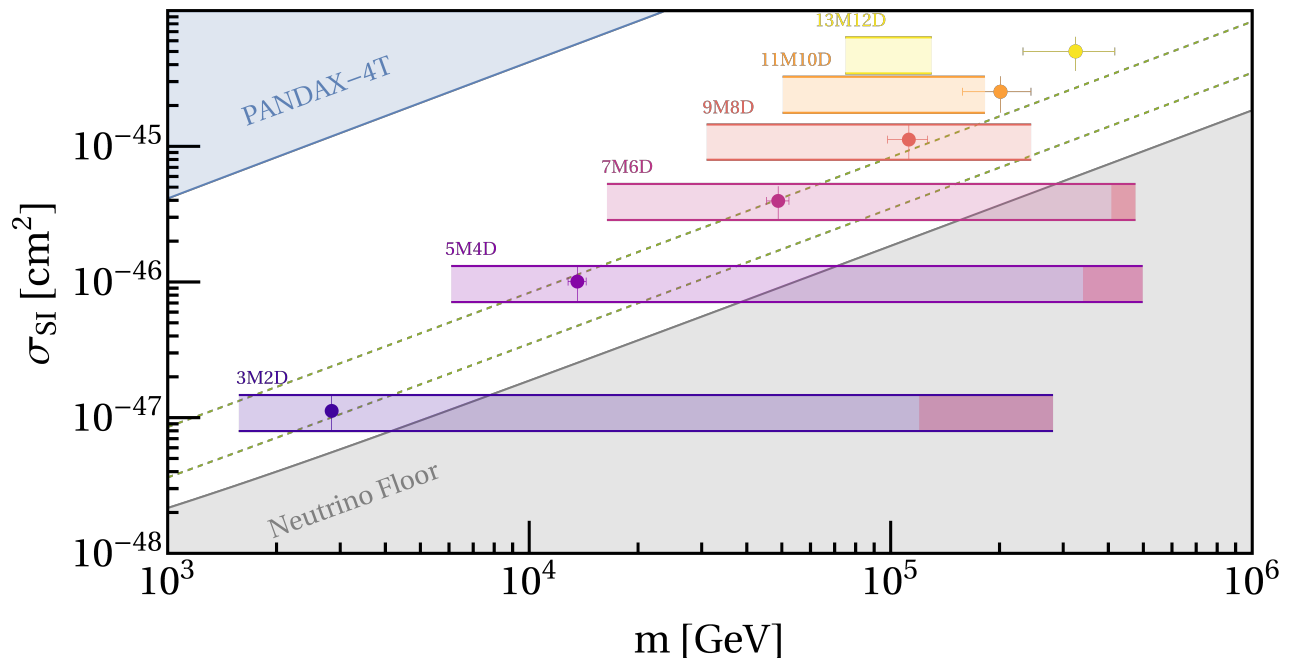


FIG. 12. Allowed parameter space of masses and spin-independent cross sections on nucleons for different multiplet combinations, shown with horizontal bands. The band thickness is determined by the lattice QCD uncertainties for the elastic cross section on nuclei [30]. Dots indicate the pure Majorana case for comparison. The red-shaded regions indicate parameter space excluded by imposing unitarity of the s -wave cross sections. The gray shaded region indicates the neutrino floor and the blue shaded region is the PandaX-4T exclusion region. The dashed green lines indicate the projected XLZD 200 and 100 ton-year $3\text{-}\sigma$ detection sensitivity [32].

Due to the phenomenological similarity between the behavior of HC-MDM and individual-multiplet MDM in the late universe when scattering on nuclei, we can easily determine the viability of detecting this particle in the next generation of direct-detection experiments. We find that the parameter space for some of the lower dimensional multiplet combinations extends beyond the reach of upcoming proposed experiments. Furthermore, the parameter space extends well below the neutrino floor, ruling out complete coverage in standard direct-detection experiments. Larger multiplet combinations, however, are well within the grasp of the next generation of experiments. We emphasize that this conclusion applies to *standard* direct-detection experiments. In principle, detectors with directional capabilities may be able to probe below the neutrino floor [58].

Ultimately, the most reliable test of any WIMP model lies in observing its annihilation products in the late universe. Furthermore, this method would evade the limitations on direct-detection experiments which make detection of low dimensional multiplets impossible. To accurately model the spectrum and composition of these annihilation products in the HC-MDM model requires a different formalism from that presented here, valid after $SU(2)_L$ symmetry breaking. This is deferred for a later paper.

There are other potential avenues for future exploration. First, in this paper we have made a series of simplifying assumptions about the magnitude of the Higgs

coupling constants of the DM multiplets as well as their individual masses. We have also neglected some of the smaller contributions to the annihilation cross section, mainly those of $\ell > 0$ states. Forgoing these simplifications increases the computational complexity, but the formalism developed here can, in principle, be extended to cover this scenario. Additionally, here we have considered large coupling values and masses that cancel the tree-level H -mediated scattering cross section contributions to direct detection of HC-MDM particles. Loop induced corrections involving H exchanges may provide extra contributions to the scattering cross section relevant for direct-detection (loops involving only gauge bosons are already taken into account following [45]). Note however that $y_1 = -y_2$ (as considered in the large coupling case) corresponds to a custodial symmetry. The symmetry is only approximate as it is explicitly broken by $U(1)_V$ interactions. However, we expect that our conclusions remain qualitatively unchanged. Ultimately, while fully probing the parameter space of HC-MDM will be challenging, it remains an essential goal.

ACKNOWLEDGMENTS

We are grateful for helpful discussions with Fareed Alasiri, Eric Braaten, Roberto Bruschini, Marco Cirelli, Sean Fleming, Richard Furnstahl, Kalliopi Petraki, Chris Hirata, Obada Nairat, Stuart Raby, Michele Redi, Diego

Redigolo, Tracy Slatyer, Alessandro Strumia, Todd Thompson, and Bryan Zaldivar.

SG and JFB were supported by National Science Foundation Grant No. PHY-2310018. JS was supported by the UK Research and Innovation Future Leader Fellowship MR/Y018656/1. LLH was supported by the Fonds de la Recherche Scientifique F.R.S.-FNRS through a senior research associate position, is a member of BLU-ULB ([Brussels Laboratory of the Universe](#)), and acknowledges the support of the FNRS research grant number J.0134.24, the ARC program of the Federation Wallonie-Bruxelles, and the IISN convention No. 4.4503.15.

Appendices

Here we collect a series of results necessary to rederive the work in the main body of the paper. Some of these details are already given in other papers referenced throughout this work, however we compile them here to aid the reader by providing a single source for all of the necessary results. We also briefly discuss our results for pure Majorana MDM and compare them to the existing literature.

In the following, we cover our results for the pure Majorana case, contraction of $SU(2)_L$ indices, the annihilation amplitudes for $DM \rightarrow SM$, and the $DM \rightarrow BS$ amplitudes.

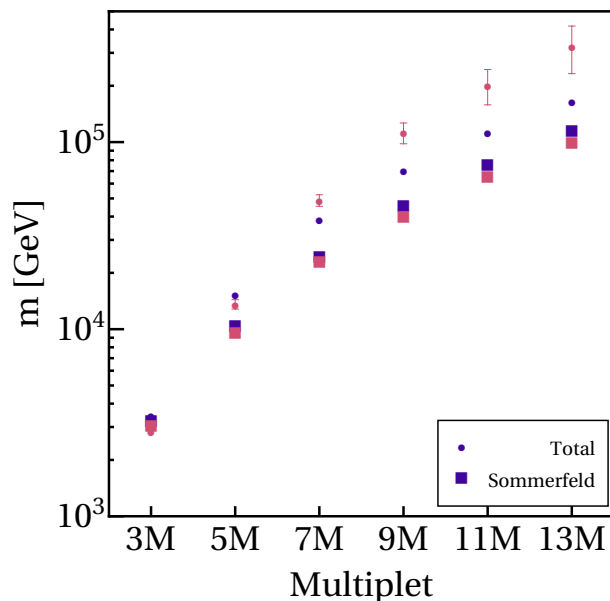


FIG. 13. Comparison of our results (blue) to Ref. [30] (pink) for pure Majorana MDM. Shown are the total masses obtained including bound states as well as the result considering Sommerfeld enhancement only.

Appendix A: Pure Majorana multiplets

We have chosen to use the results of Ref. [30] for the pure Majorana case in this paper. As mentioned in Sec. VII, we only consider a subset of possible bound states in our calculation of the DM mass. This is due to the computational cost associated with the mixed-multiplet calculation, which quickly grows with larger multiplets. The result is an underestimation of the effective annihilation cross section, and therefore the DM mass. For completeness, we compare our results for pure Majorana MDM with those of Ref. [30].

Figure 13 compares our results (blue) for the DM mass giving rise to the right relic abundance to those of Ref. [30] (pink) with (dots) and without (squares) bound states. We see that when we only consider Sommerfeld enhancement, we have excellent agreement with Ref. [30]. When we consider bound states, we find that for smaller multiplets we again agree completely with their results. As the multiplet size grows, we begin to underestimate the mass. This is due to the increasing number of available bound states as well as their growing binding energy taken into account in [30], which makes our truncation more severe. However, even in the 13-plet, where this error is greatest, we only underpredict the Bottaro et al. result by $\sim 30\%$.

Appendix B: Contracting indices

Here we demonstrate the origin of the $\hat{\epsilon}_X$ operator used to contract two $SU(2)_L$ multiplets given in Sec. II and used throughout the paper. We use a quadruplet X with $Y_X = 1/2$ for this example. We can represent X, \bar{X} in two different ways. The first is

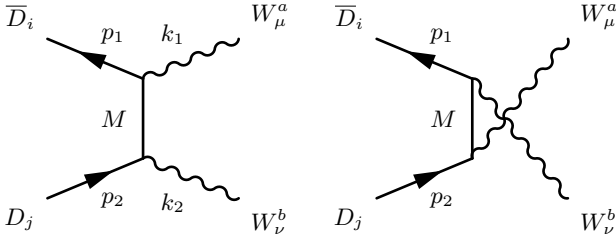
$$X = \begin{pmatrix} X^{++} \\ X^+ \\ X^0 \\ X^- \end{pmatrix}, \quad \bar{X} = \begin{pmatrix} \bar{X}^+ \\ \bar{X}^0 \\ \bar{X}^- \\ \bar{X}^{--} \end{pmatrix}, \quad (\text{B1})$$

where the superscripts indicate the electric charge from Eq. (2).

We can also represent the multiplet by a totally symmetric tensor with 3 indices

$$X = \begin{pmatrix} X_{111} \\ \sqrt{3}X_{112} \\ \sqrt{3}X_{122} \\ X_{222} \end{pmatrix}, \quad \bar{X} = \begin{pmatrix} \bar{X}_{111} \\ \sqrt{3}\bar{X}_{112} \\ \sqrt{3}\bar{X}_{122} \\ \bar{X}_{222} \end{pmatrix}. \quad (\text{B2})$$

It is then straightforward to contract $\bar{X}X$ using the

FIG. 14. Diagrams for $D\bar{D}$ annihilation to WW .

$SU(2)_L$ invariant Levi-Civita symbol ϵ_{ij}

$$\begin{aligned}
\bar{X}X &= \bar{X}_{ijk}X_{i'j'k'}\epsilon^{ii'}\epsilon^{jj'}\epsilon^{kk'} \\
&= \bar{X}_{111}X_{222} - (\bar{X}_{112}X_{221} + \bar{X}_{121}X_{212} + \bar{X}_{211}X_{122}) \\
&\quad + (\bar{X}_{122}X_{211} + \bar{X}_{212}X_{121} + \bar{X}_{221}X_{112}) - \bar{X}_{222}X_{111} \\
&= \bar{X}^+X^- - \bar{X}^0X^0 + \bar{X}^-X^+ - \bar{X}^{--}X^{++}.
\end{aligned} \tag{B3}$$

Defining the matrix

$$\hat{\epsilon}_4 = \begin{pmatrix} 0 & 0 & 0 & 1 \\ 0 & 0 & -1 & 0 \\ 0 & 1 & 0 & 0 \\ -1 & 0 & 0 & 0 \end{pmatrix} \tag{B4}$$

we see that

$$\bar{X}X = \bar{X} \cdot \hat{\epsilon}_4 X. \tag{B5}$$

We can generalize this to any dimension R (written as $\hat{\epsilon}_R$). Essentially, $\hat{\epsilon}_R$ flips the order of the multiplet to form gauge invariant combinations. We frequently make use of the fact that $\hat{\epsilon}_R \hat{\epsilon}_R^T = 1$.

For example, we wish to decompose the process $\bar{D}_i D_j \rightarrow WW$ into isospin contributions. Using CG coefficients,

$$\begin{aligned}
\mathcal{M} &\propto \langle I_{IS}, M_{IS} | I_D, I_D^3(i); I_D, I_D^3(j) \rangle (\hat{\epsilon}_D)_{ik} (t_D^a)_{kl} (t_D^b)_{lj} \\
&= \langle IS \rangle_{ij} (\hat{\epsilon}_D t_D^a t_D^b)_{ij},
\end{aligned} \tag{B6}$$

where in the second line we have used a shorthand notation for the CG coefficients.

Appendix C: Annihilation amplitudes

In this appendix we derive the amplitudes used in the cross sections in Sec. IV. Throughout, we use the non-relativistic spinor approximations

$$u(p) \rightarrow \sqrt{m} \begin{pmatrix} \xi \\ \xi \end{pmatrix}, \quad v(p) \rightarrow \sqrt{m} \begin{pmatrix} \xi \\ -\xi \end{pmatrix}. \tag{C1}$$

1. $D\bar{D} \rightarrow WW$

In the non-relativistic limit with massless vector bosons, the kinematics are (see Fig. 14):

$$\begin{aligned}
p_1 &\approx (m, \vec{0}), & k_1 &\approx (m, 0, 0, m) \\
P_2 &\approx (m, \vec{0}), & k_2 &\approx (m, 0, 0, -m).
\end{aligned} \tag{C2}$$

This leads to the simplifications

$$\not{p}_1 - \not{k}_1 \rightarrow m \begin{pmatrix} 0 & \sigma^3 \\ -\sigma^3 & 0 \end{pmatrix}, \quad (p_1 - k_1)^2 \rightarrow -m^2. \tag{C3}$$

For the t -channel $D\bar{D}$ annihilation to WW process, the amplitude is

$$\begin{aligned}
i\mathcal{M}_t &= \\
&(ig_2)^2 \epsilon_\mu^{a*}(k_1) \epsilon_\nu^{b*}(k_2) \bar{v}(p_1) t_D^a \gamma^\mu \frac{i(\not{p}_1 - \not{k}_1 + m)}{(p_1 - k_1)^2 - m^2} t_D^b \gamma^\nu u(p_2).
\end{aligned} \tag{C4}$$

Explicitly writing the $SU(2)_L$ indices, this has the structure

$$\bar{v}_i (\hat{\epsilon}_D)_{ij} (t_D^a)_{jk} (t_D^b)_{kl} u_l. \tag{C5}$$

We can decompose this into isospins by letting

$$G_{D\bar{D};WW}^{ab} = \langle I_{IS}, M_{IS} | I_D, I_D^3(i); I_D, I_D^3(j) \rangle (\hat{\epsilon}_D t_D^a t_D^b)_{ij}, \tag{C6}$$

where we have used the contraction operator from Appendix B.

Applying the non-relativistic simplifications and using $\epsilon_0^a = \epsilon_0^b = 0$,

$$i\mathcal{M}_t = -i(ig_2)^2 \text{Tr}(\sigma^i \sigma^3 \sigma^j \xi \xi'^{\dagger}) \epsilon_i^{a*}(k_1) \epsilon_j^{b*}(k_2) G_{D\bar{D};WW}^{ab} \tag{C7}$$

For the spin zero configuration, $\xi \xi'^{\dagger} = (1/\sqrt{2})\mathbf{1}$, where $\mathbf{1}$ is the 2×2 identity matrix (see Ref. [53]). Using

$$\pm \epsilon^a(k_1) = \frac{1}{\sqrt{2}}(0, 1, \pm i, 0), \quad \pm \epsilon^b(k_2) = \frac{1}{\sqrt{2}}(0, -1, \pm i, 0), \tag{C8}$$

we obtain the amplitudes

$$\begin{aligned}
\mathcal{M}_{t,+ -} &= \mathcal{M}_{t,- +} = 0 \\
\mathcal{M}_{t,+ +} &= -\mathcal{M}_{t,- -} = \sqrt{2}(ig_w)^2 G_{D\bar{D};WW}^{ab}
\end{aligned} \tag{C9}$$

For the u -channel, $t^a \leftrightarrow t^b$ so $G_{D\bar{D};WW}^{ab} \rightarrow G_{D\bar{D};WW}^{ba}$, $\mu \leftrightarrow \nu$ in the γ matrices, and $\not{p}_1 - \not{k}_1 \rightarrow \not{p}_1 - \not{k}_2 = -(\not{p}_1 - \not{k}_1)$. Adding both diagrams,

$$|\mathcal{M}|^2 = 4g_2^4 (G_{D\bar{D};WW}^{ab} + G_{D\bar{D};WW}^{ba})^2. \tag{C10}$$

From the Landau-Yang theorem, this process only occurs with spin zero [29]. WW must have $R_{FS} = 1, 3, 5$, but for $R = 3$ the gauge factor combination vanishes. So this process occurs in spin-0, $R_{IS} = 1, 5$ states.

2. $D\bar{D} \rightarrow HH^*$

The t -channel process of $D\bar{D} \rightarrow HH^*$ shares the same kinematics and approximations as the $D\bar{D} \rightarrow WW$ case. The amplitude is

$$i\mathcal{M} = -iy_1 y_2 \text{Tr}(\sigma^3 \xi \xi'^{\dagger}). \quad (\text{C11})$$

For spin zero, $\xi \xi'^{\dagger} \propto \mathbf{1}$ and \mathcal{M} vanishes.

For spin one, $\xi \xi'^{\dagger} = (\vec{n}^* \cdot \vec{\sigma})/\sqrt{2}$, where \vec{n} are the three bound state polarization vectors. This is only non-zero for the transverse polarization so

$$i\mathcal{M} = -i2\sqrt{2}y_1 y_2. \quad (\text{C12})$$

Because isospin is conserved, this process occurs for spin one, $R_{BS} = 1, 3$.

The s -channel process $D\bar{D} \rightarrow W \rightarrow HH^*$ is easiest to account for by adding it to the $D\bar{D} \rightarrow W \rightarrow f\bar{f}$ case considered below.

3. $D\bar{D} \rightarrow f\bar{f}$

$D\bar{D} \rightarrow f\bar{f}$ occurs through an s -channel process mediated by the W . Requiring isospin and spin conservation, this only occurs with $I_{BS} = 1, s_{BS} = 1$. Because I_{BS} is restricted to one value, we do not need to decompose the process using CG coefficients.

Defining

$$G_{D\bar{D};f\bar{f}} = \text{Tr}(t_D^a t_D^b) \text{Tr}(t_{SM}^a t_{SM}^b), \quad (\text{C13})$$

the amplitude is

$$i\mathcal{M} = (ig_2)^2 \bar{v} \gamma^\mu u \frac{-ig_{\mu\nu}}{q^2} \bar{u} \gamma^\nu v G_{D\bar{D};f\bar{f}}, \quad (\text{C14})$$

where q is the W momentum and we have omitted the fermion momenta.

Because the process is mediated by the W , f must be left-handed and \bar{f} right-handed. Using the familiar non-relativistic approximations,

$$\mathcal{M} = 2(ig_2)^2 G_{D\bar{D};f\bar{f}}. \quad (\text{C15})$$

When we compute the cross section from this amplitude, we multiply by the number of fermions, $n_f = 12$. However, we can account for the process $D\bar{D} \rightarrow W \rightarrow HH^*$ by replacing $n_f \rightarrow n_p = 25/2$, as noted in Sec. IV.

4. $MM \rightarrow WW$

We can read off the $MM \rightarrow WW$ amplitude from the $D\bar{D} \rightarrow WW$ one. We define $G_{MM;WW}^{ab}$ as in the $D\bar{D}$ case and note that we obtain an additional symmetry factor of $1/2$ in the cross section.

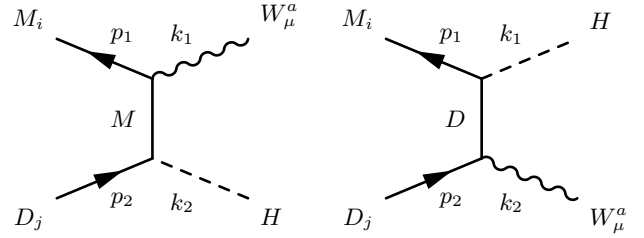


FIG. 15. Diagrams for MD annihilation to HW .

5. $MM \rightarrow HH^*$

The $MM \rightarrow HH^*$ can be determined from the $D\bar{D}$ case. We now have a u -channel diagram which has a relative minus from fermion exchange and an additional minus from $\not{p}_1 - \not{k}_1 \rightarrow \not{p}_1 - \not{k}_2$, so the diagrams add together. We also get a symmetry factor of $1/2$ from the identical particles, so overall the cross section is double the $D\bar{D}$ cross section.

6. $MM \rightarrow f\bar{f}$

The $MM \rightarrow f\bar{f}$ amplitude is found by comparison to the $D\bar{D} \rightarrow f\bar{f}$ case. We define $G_{MM;f\bar{f}}$ as in the the $D\bar{D}$ case and multiply the cross section by the symmetry factor of $1/2$.

7. $DD/\bar{D}\bar{D} \rightarrow HH$

The $DD/\bar{D}\bar{D} \rightarrow HH$ is found from the $MM \rightarrow HH^*$ example. In this case we have identical particles in the initial and final states, so the cross section gets a factor of $1/2$ compared to the MM cross section

8. $MD/\bar{D} \rightarrow WH/H^*$

Figure 15 shows the diagrams for the $MD \rightarrow WH/H^*$ case. Writing the $SU(2)_L$ indices explicitly, the diagram on the left has the structure

$$i\mathcal{M} \propto \bar{v}_i (\hat{\epsilon}_M^a)_{ij} (t_M^a)_{jk} \delta_{I_M^3(k) \pm 1/2} I_M^3(l) u_l, \quad (\text{C16})$$

where we have omitted the momenta arguments. Defining

$$\pm G_{MD;WH} = \langle I_{IS}, M_{IS} | I_M, I_M^3(i); I_D, I_M^3(j) \pm 1/2 \rangle (\hat{\epsilon}_M^a)_{ij}, \quad (\text{C17})$$

and using the non-relativistic approximations

$$i\mathcal{M} = -ig_2 y_1 \epsilon_n^*(k_1) \text{Tr}(\sigma^n \xi \xi'^{\dagger}) \pm G_{MD;WH}. \quad (\text{C18})$$

In spin zero, this vanishes. In spin-1, using L, R to denote the W handedness and $1, 2$ for the initial state polarization,

$$\mathcal{M}^{R,2} = \mathcal{M}^{L,1} = g_2 y_1 \sqrt{2} \pm G_{MD;WH}. \quad (\text{C19})$$

The diagram on the right in Fig. 15 produces the same amplitude with the substitution $\pm_1 G_{MD;WH} \rightarrow \pm_2 G_{MD;WH}$,

$$\pm_2 G_{MD;WH} = \langle I_{IS}, M_{IS} | I_M, I_D^3(i) \pm 1/2; I_D, I_D^3(j) \rangle (t_D^a)_{ij}. \quad (\text{C20})$$

Adding the two diagrams together leads to the cross section in Eq. (41). Note that when the gauge factor is squared, we sum over the $+$, $-$ as indices.

9. $MD/\overline{D} \rightarrow H/H^* \rightarrow SM$

In unbroken $SU(2)_L$, the H does not couple to WW (we can also note that isospin could not be conserved in the process) so the relevant process is $MD/\overline{D} \rightarrow H/H^* \rightarrow f\overline{f}$. However, in the non-relativistic limit this is also zero.

Appendix D: Bound-state formation amplitudes

Here we derive the amplitudes used in the calculation of bound-state formation cross sections in Sec. VI.

We use $\phi_{p\ell,ij}$ for the scattering state wavefunctions and $\psi_{n'\ell'm',i'j'}$ for the bound state wavefunctions. Here p, ℓ are the momentum and angular momentum of the scattering state, $n\ell m$ are the quantum numbers of the bound state, and i, j are $SU(2)_L$ indices. Bound state indices are primed and scattering states unprimed. The radial part of the bound state wavefunction is given in Eq. (74)

The radial part of the scattering state wavefunction in the massless vector limit is approximated by

$$R_\ell(r) = \frac{\sqrt{4\pi(2\ell+1)S}}{\Gamma(2\ell+2)} e^{-ipr} (2pr)^\ell$$

$$F_1 \left(\ell + 1 \frac{i\alpha_{\text{eff}}}{v_{\text{rel}}}, 2\ell + 2, 2ipr \right) \prod_{n=1}^{\ell} \left(\ell - n + 1 - \frac{i\alpha_{\text{eff}}}{v_{\text{rel}}} \right), \quad (\text{D1})$$

where F is the hypergeometric function and S is the Sommerfeld factor. This approximation requires an additional correction for states with $\ell \neq 0$, which is the case when we consider formation of $\ell = 0$ bound states from $\ell = 1$ scattering states through W, B emission. The correction multiplies the resulting cross sections by

$$L_\ell = \frac{w^{2\ell}}{\prod_{k=0}^{\ell-1} ((\ell-k)^2 + w^2)} \quad \text{with} \quad w = \frac{mv_{\text{rel}}}{\kappa m_V}, \quad (\text{D2})$$

where m_V is the relevant vector boson mass and $\kappa \approx 1.74$ arises from the Hulthen potential used to derive the Sommerfeld factor in the case of massive vector bosons [29].

We make use of the non-relativistic approximations

$$\begin{aligned} \bar{u}_i(p') u_j(p) &\rightarrow 2m \delta_{ij} \\ \bar{u}_i(p') \gamma^\mu u_j(p) &\rightarrow (2m \delta^{\mu 0} + (\vec{p}' + \vec{p})_k \delta^{\mu k}) \delta_{ij} \\ \bar{u}_i(p') \gamma^\mu t_{ij}^a u_j(p) &\rightarrow (2m \delta^{\mu 0} + (\vec{p}' + \vec{p})_k \delta^{\mu k}) t_{ij}^a, \end{aligned} \quad (\text{D3})$$

where k is a vector index and we have suppressed the spin indices because they are individually conserved. We have been slightly careless with the $SU(2)_L$ indices in the last expression, but these indices are contracted with the overlap integrals shown below. We also use the overlap integrals

$$\begin{aligned} \vec{J}_{p,n\ell m}^{ij,i'j'} &= \int d^3r \psi_{i'j'}^* \nabla \phi_{ij} \\ \vec{T}_{p,n\ell m}^{ij,i'j'} &= \frac{\alpha_2 m}{2} \int d^3r \psi_{i'j'}^* \hat{r} \phi_{ij} \\ \vec{F}_{p,n\ell m}^{ij,i'j'} &= \frac{m}{2} \int d^3r \psi_{i'j'}^* \phi_{ij}, \end{aligned} \quad (\text{D4})$$

where we have omitted indices on the wavefunctions for convenience and use the kinematics (see Fig. 3)

$$\begin{aligned} \vec{P} &= \vec{p}_1 + \vec{p}_2, & \vec{K} &= \vec{k}_1 + \vec{k}_2 \\ \vec{p}_1 &= \frac{\vec{P}}{2} + \vec{p}, & \vec{k}_1 &= \frac{\vec{K}}{2} + \vec{k} \\ \vec{p}_2 &= \frac{\vec{P}}{2} - \vec{p}, & \vec{k}_2 &= \frac{\vec{K}}{2} - \vec{k}. \end{aligned} \quad (\text{D5})$$

1. W/B emission

For the W/B emission diagram in the top left of Fig. 3,

$$\begin{aligned} i\mathcal{M} &= \bar{u}_{j'}(k_2) (\hat{\epsilon}_{X_2})_{j'j} u_j(p_2) \bar{u}_{i'}(k_1) \\ &\quad (ig_2 (t_{X_1}^a)_{i'k} (\hat{\epsilon}_{X_1})_{ki} + ig_1 Y_{X_1} (\hat{\epsilon}_{X_1})_{i'i}) \gamma^\mu u_i(p_1) \epsilon_\mu^*(q). \end{aligned} \quad (\text{D6})$$

We only need the spatial part of \mathcal{M}^μ . Using the non-relativistic approximations and dressing with the scattering and bound state wavefunctions

$$\begin{aligned} \vec{\mathcal{M}} &= 2m (g_2 (t_{X_1}^a)_{i'k} (\hat{\epsilon}_{X_1})_{ki} + g_1 Y_{X_1} (\hat{\epsilon}_{X_1})_{i'i}) (\hat{\epsilon}_{X_2})_{j'j} \frac{1}{\sqrt{m}} \\ &\quad \int \frac{d^3\vec{k}}{(2\pi)^3} \frac{d^3\vec{p}}{(2\pi)^3} \psi_{i'j'}^*(\vec{k}) (\vec{p} + \vec{k}) \phi_{ij}(\vec{p}) \delta(\vec{p}_2 - \vec{k}_2) (2\pi)^3. \end{aligned} \quad (\text{D7})$$

Because $|\vec{q}|$ is small, $\vec{P} \approx \vec{K}$ so

$$\begin{aligned} \vec{\mathcal{M}} &\rightarrow 4\sqrt{m} (g_2 (t_{X_1}^a)_{i'k} (\hat{\epsilon}_{X_1})_{ki} + g_1 Y_{X_1} (\hat{\epsilon}_{X_1})_{i'i}) (\hat{\epsilon}_{X_2})_{j'j} \\ &\quad \int \frac{d^3p}{(2\pi)^3} \psi_{i'j'}^*(\vec{p}) \vec{p} \phi_{ij}(\vec{p}). \end{aligned} \quad (\text{D8})$$

Fourier transforming gives us our result

$$\begin{aligned} \vec{\mathcal{M}} &\rightarrow -4i\sqrt{m} (g_2 (t_{X_1}^a)_{i'k} (\hat{\epsilon}_{X_1})_{ki} + g_1 Y_{X_1} (\hat{\epsilon}_{X_1})_{i'i}) \\ &\quad (\hat{\epsilon}_{X_2})_{j'j} \vec{J}_{p,n'\ell'm'}^{ij,i'j'}. \end{aligned} \quad (\text{D9})$$

For emission from the X_2 leg of the diagram (the top right of Fig. 3, we have $\vec{p}_1 + \vec{k}_1 \rightarrow \vec{p}_2 + \vec{k}_2 = -(\vec{p} + \vec{k})$. The

δ -function argument gets an overall negative sign, but this does not change the result because the relative sign between \vec{p} and \vec{k} is unchanged. So the result is given by Eq. (D9) with an overall minus, appropriately changing $SU(2)_L$ indices, and $Y_{X_1} \rightarrow Y_{X_2}$.

When $X_1 = X_2$, we also have u -channel diagrams. This introduces a relative minus sign between arguments in the δ -function so $\psi^*(\vec{p}) \rightarrow \psi^*(-\vec{p})$ in Eq. (D8). The effect on the cross section from the symmetries of the wavefunction are discussed in Sec. VI.

We can also emit a W boson through the three boson coupling in the bottom of Fig. 3. This amplitude, when simplified to the non-relativistic limit and dressed with the scattering and bound state wavefunctions is

$$i\vec{\mathcal{M}} = i8\sqrt{m}g_2(t_{X_1}^b)_{i'k}(\hat{\epsilon}_{X_1})_{ki}(t_{X_2}^c)_{j'l}(\hat{\epsilon}_{X_2})_{lj}f^{abc}\vec{T}_{p,n'l'm'}^{ij,i'j'}. \quad (\text{D10})$$

2. H emission

For the H emission diagram on the left in Fig. 4,

$$i\mathcal{M} = (-iy_1)\bar{u}_{j'}(k_2)u_j(p_2)(\hat{\epsilon}_M)_{j'j}\bar{u}_{i'}(k_1)u_i(p_1)(\hat{\epsilon}_D)_{ki}\delta_{I_D^3(k)\pm 1/2}^{I_M^3(i')}. \quad (\text{D11})$$

Dressing with the scattering and bound state wavefunctions and using non-relativistic approximations, we have

$$i\mathcal{M} = -iy_1 4m^2(\hat{\epsilon}_D)_{ki}\delta_{I_D^3(k)\pm 1/2}^{I_M^3(i')}(\hat{\epsilon}_M)_{j'j}\frac{1}{\sqrt{m}} \int \frac{d^3p}{(2\pi)^3} \frac{d^3k}{(2\pi)^3} \psi_{i'j'}^*(\vec{k})\phi_{ij}(\vec{p})\delta(\vec{p}_2 - \vec{k}_2)(2\pi)^3. \quad (\text{D12})$$

Using the small $|\vec{q}|$ approximation and Fourier transforming to position space

$$i\mathcal{M} = -8iy_1\sqrt{m}(\hat{\epsilon}_D)_{ki}\delta_{I_D^3(k)\pm 1/2}^{I_M^3(i')}(\hat{\epsilon}_M)_{j'j}F_{p,n'l'm'}^{ij,i'j'}. \quad (\text{D13})$$

Swapping $M \rightleftharpoons D, H \rightarrow H^*$ changes $y_1 \rightarrow y_2$ in Eq. (D13). However, this has no effect when we square the amplitude because $|y_1| = |y_2|$. Emitting from the $p_2 \rightarrow k_2$ leg only changes the overall sign of the δ -function argument, so this also has no effect on the amplitude. When we have u -channel diagrams, the relative sign in the δ -function argument changes. This changes the sign of the argument of the BS wavefunction, ψ , and we obtain the symmetry factors discussed in Sec. VI.

Figure 16 shows a diagram which also produces bound states through H emission, however it is suppressed by higher orders of the coupling constants [36]. Therefore we ignore this bound-state formation mechanism.

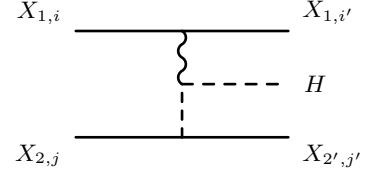


FIG. 16. Bound-state formation with Higgs emission and scalar vector fusion.

- [1] G. Bertone and D. Hooper, *Reviews of Modern Physics* **90** (2018), 10.1103/revmodphys.90.045002.
- [2] B. Carr, M. Raidal, T. Tenkanen, V. Vaskonen, and H. Veermäe, *Phys. Rev. D* **96**, 023514 (2017), arXiv:1705.05567 [astro-ph.CO].
- [3] S. Ge, K. Lawson, and A. Zhitnitsky, *Phys. Rev. D* **99**, 116017 (2019), arXiv:1903.05090 [hep-ph].
- [4] M. Cirelli, Y. Gouttenoire, K. Petraki, and F. Sala, *JCAP* **02**, 014 (2019), arXiv:1811.03608 [hep-ph].
- [5] J. Berges, A. Chatrchyan, and J. Jaeckel, *JCAP* **08**, 020 (2019), arXiv:1903.03116 [hep-ph].
- [6] M. Blennow, E. Fernandez-Martinez, A. Olivares-Del Campo, S. Pascoli, S. Rosauero-Alcaraz, and A. V. Titov, *Eur. Phys. J. C* **79**, 555 (2019), arXiv:1903.00006 [hep-ph].
- [7] G. Arcadi, A. Djouadi, and M. Raidal, *Phys. Rept.* **842**, 1 (2020), arXiv:1903.03616 [hep-ph].
- [8] S. W. Allen, A. E. Evrard, and A. B. Mantz, *Ann. Rev. Astron. Astrophys.* **49**, 409 (2011), arXiv:1103.4829 [astro-ph.CO].
- [9] P. Salucci, *Astron. Astrophys. Rev.* **27**, 2 (2019), arXiv:1811.08843 [astro-ph.GA].
- [10] N. Aghanim *et al.* (Planck), *Astron. Astrophys.* **641**, A6 (2020), [Erratum: *Astron. Astrophys.* 652, C4 (2021)], arXiv:1807.06209 [astro-ph.CO].
- [11] J. D. Simon, *Ann. Rev. Astron. Astrophys.* **57**, 375 (2019), arXiv:1901.05465 [astro-ph.GA].
- [12] M. Cirelli, A. Strumia, and J. Zupan, (2024), arXiv:2406.01705 [hep-ph].
- [13] M. Cirelli, N. Fornengo, and A. Strumia, *Nucl. Phys. B* **753**, 178 (2006), arXiv:hep-ph/0512090.
- [14] M. Cirelli, A. Strumia, and M. Tamburini, *Nucl. Phys. B* **787**, 152 (2007), arXiv:0706.4071 [hep-ph].
- [15] G. Steigman and M. S. Turner, *Nucl. Phys. B* **253**, 375 (1985).
- [16] G. Bertone, D. Hooper, and J. Silk, *Phys. Rept.* **405**, 279 (2005), arXiv:hep-ph/0404175.
- [17] G. Steigman, B. Dasgupta, and J. F. Beacom, *Phys. Rev. D* **86**, 023506 (2012), arXiv:1204.3622 [hep-ph].
- [18] G. Arcadi, M. Dutra, P. Ghosh, M. Lindner, Y. Mambrini, M. Pierre, S. Profumo, and F. S. Queiroz, *Eur. Phys. J. C* **78**, 203 (2018), arXiv:1703.07364 [hep-ph].
- [19] L. Roszkowski, E. M. Sessolo, and S. Trojanowski, *Rept. Prog. Phys.* **81**, 066201 (2018), arXiv:1707.06277 [hep-ph].
- [20] J. Smirnov, *SciPost Phys. Proc.* **12**, 003 (2023), arXiv:2212.14361 [hep-ph].
- [21] J. Hisano, S. Matsumoto, and M. M. Nojiri, *Phys. Rev. Lett.* **92**, 031303 (2004), arXiv:hep-ph/0307216.
- [22] J. Hisano, S. Matsumoto, M. M. Nojiri, and O. Saito, *Phys. Rev. D* **71**, 063528 (2005), arXiv:hep-ph/0412403.
- [23] J. Hisano, S. Matsumoto, M. Nagai, O. Saito, and M. Senami, *Phys. Lett. B* **646**, 34 (2007), arXiv:hep-ph/0610249.
- [24] N. Arkani-Hamed, D. P. Finkbeiner, T. R. Slatyer, and N. Weiner, *Phys. Rev. D* **79**, 015014 (2009), arXiv:0810.0713 [hep-ph].
- [25] S. Cassel, *J. Phys. G* **37**, 105009 (2010), arXiv:0903.5307 [hep-ph].
- [26] J. D. March-Russell and S. M. West, *Phys. Lett. B* **676**, 133 (2009), arXiv:0812.0559 [astro-ph].
- [27] B. von Harling and K. Petraki, *JCAP* **12**, 033 (2014), arXiv:1407.7874 [hep-ph].
- [28] H. An, M. B. Wise, and Y. Zhang, *Phys. Rev. D* **93**, 115020 (2016), arXiv:1604.01776 [hep-ph].
- [29] A. Mitridate, M. Redi, J. Smirnov, and A. Strumia, *JCAP* **05**, 006 (2017), arXiv:1702.01141 [hep-ph].
- [30] S. Bottaro, D. Buttazzo, M. Costa, R. Franceschini, P. Panci, D. Redigolo, and L. Vittorio, *Eur. Phys. J. C* **82**, 31 (2022), arXiv:2107.09688 [hep-ph].
- [31] I. M. Bloch, S. Bottaro, D. Redigolo, and L. Vittorio, *JHEP* **08**, 216 (2025), arXiv:2410.02723 [hep-ph].
- [32] J. Aalbers *et al.* (XLZD), (2024), arXiv:2410.17137 [hep-ex].
- [33] M. W. Goodman and E. Witten, *Phys. Rev. D* **31**, 3059 (1985).
- [34] D. S. Akerib *et al.* (CDMS), *Phys. Rev. Lett.* **96**, 011302 (2006), arXiv:astro-ph/0509259.
- [35] L. Lopez Honorez, M. H. G. Tytgat, P. Tziveloglou, and B. Zaldivar, *JHEP* **04**, 011 (2018), arXiv:1711.08619 [hep-ph].
- [36] R. Oncala and K. Petraki, *JHEP* **06**, 124 (2021), arXiv:2101.08666 [hep-ph].
- [37] R. Oncala and K. Petraki, *JHEP* **08**, 069 (2021), arXiv:2101.08667 [hep-ph].
- [38] P. Asadi, M. Baumgart, P. J. Fitzpatrick, E. Krupczak, and T. R. Slatyer, *JCAP* **02**, 005 (2017), arXiv:1610.07617 [hep-ph].
- [39] J. Smirnov and J. F. Beacom, *Phys. Rev. D* **100**, 043029 (2019), arXiv:1904.11503 [hep-ph].
- [40] T. Hambye, F. S. Ling, L. Lopez Honorez, and J. Rocher, *JHEP* **07**, 090 (2009), [Erratum: *JHEP* 05, 066 (2010)], arXiv:0903.4010 [hep-ph].
- [41] J. Billard, L. Strigari, and E. Figueroa-Feliciano, *Phys. Rev. D* **89**, 023524 (2014), arXiv:1307.5458 [hep-ph].
- [42] B. R. Safdi and W. L. Xu, (2025), arXiv:2507.15934 [hep-ph].
- [43] M. Aghaie, A. Donarini, G. Marino, and P. Panci, (2025), arXiv:2507.17607 [hep-ph].
- [44] M. Baumgart, S. Bottaro, D. Redigolo, N. L. Rodd, and T. R. Slatyer, (2025), arXiv:2507.15937 [hep-ph].
- [45] J. Hisano, K. Ishiwata, and N. Nagata, *JHEP* **06**, 097 (2015), arXiv:1504.00915 [hep-ph].
- [46] T. Cohen, J. Kearney, A. Pierce, and D. Tucker-Smith, *Phys. Rev. D* **85**, 075003 (2012), arXiv:1109.2604 [hep-ph].
- [47] C. Cheung and D. Sanford, *JCAP* **02**, 011 (2014), arXiv:1311.5896 [hep-ph].
- [48] L. Calibbi, A. Mariotti, and P. Tziveloglou, *JHEP* **10**, 116 (2015), arXiv:1505.03867 [hep-ph].
- [49] A. Mitridate, M. Redi, J. Smirnov, and A. Strumia, *JHEP* **10**, 210 (2017), arXiv:1707.05380 [hep-ph].
- [50] N. A. Dondi, F. Sannino, and J. Smirnov, *Phys. Rev. D* **101**, 103010 (2020), arXiv:1905.08810 [hep-ph].
- [51] M. Garny and J. Heisig, *Phys. Rev. D* **105**, 055004 (2022), arXiv:2112.01499 [hep-ph].
- [52] S. Navas *et al.* (Particle Data Group), *Phys. Rev. D* **110**, 030001 (2024).
- [53] M. E. Peskin and D. V. Schroeder, *An Introduction to quantum field theory* (Addison-Wesley, Reading, USA, 1995).
- [54] L. Schiff, *Quantum Mechanics: 3rd Edition* (McGraw

- Hill, 1968).
- [55] C. Cohen-Tannoudji, B. Diu, and F. Laloë, *Quantum Mechanics, Volume 2: Angular Momentum, Spin, and Approximation Methods* (Wiley, 2019).
- [56] H. A. Bethe and E. E. Salpeter, *Quantum Mechanics of One and Two-Electron Atoms* (Springer Berlin, Heidelberg, 1957).
- [57] K. Griest and D. Seckel, *Phys. Rev. D* **43**, 3191 (1991).
- [58] J. Billard, F. Mayet, and D. Santos, *Phys. Rev. D* **85**, 035006 (2012), [arXiv:1110.6079 \[astro-ph.CO\]](https://arxiv.org/abs/1110.6079).